University of Massachusetts Amherst

ScholarWorks@UMass Amherst

April 2021

Correcting For Terrain Interference, Attenuation, and System Bias for a Dual Polarimetric, X-Band Radar

Casey Wolsieffer
University of Massachusetts Amherst

University of Massachusetts Amherst

ScholarWorks@UMass Amherst

Masters Theses   Dissertations and Theses

Correcting For Terrain Interference, Attenuation, and System Bias for a Dual Polarimetric, X-Band Radar

Casey Wolsieffer

CORRECTING FOR TERRAIN INTERFERENCE, ATTENUATION, AND SYSTEM BIAS FOR A DUAL POLARIMETRIC, X-BAND RADAR

A Thesis Presented

by

CASEY WOLSIEFFER

Submitted to the Graduate School of the
University of Massachusetts Amherst in partial fulfillment
of the requirements for the degree of

MASTER OF SCIENCE IN ELECTRICAL AND COMPUTER ENGINEERING

February 2021

Electrical and Computer Engineering

CORRECTING FOR TERRAIN INTERFERENCE, ATTENUATION, AND SYSTEM BIAS FOR A DUAL POLARIMETRIC, X-BAND RADAR

A Thesis Presented

by

CASEY WOLSIEFFER

Approved as to style and content by:

_____

Stephen Frasier, Chair

_____

Paul Siqueira, Member

_____

Do-Hoon Kwon, Member

_____

Michael Zink, Member

_____

Christopher V. Hollot, Department Head
Electrical Engineering

ABSTRACT

CORRECTING FOR TERRAIN INTERFERENCE, ATTENUATION, AND SYSTEM BIAS FOR A DUAL POLARIMETRIC, X-BAND RADAR

FEBRUARY 2021

CASEY WOLSIEFFER, B.S., UNIVERSITY OF MASSACHUSETTS AMHERST

M.S.E.C.E., UNIVERSI TY OF MASSACHUSETTS AMHERST

Directed by: Professor Stephen Frasier

This thesis outlines the procedure and theory used to calibrate the UMass eX-perimental X-band Radar (UMAXX) for the purpose of monitoring meteorological events in the Pioneer Valley region. Due to the complex topography of the area, lower tilt angles are subject to partial or full beam blockage as well as ground clutter observed through the main beam or sidelobes. Additionally, there are biases internal and external to the system that impact the reflectivity and differential reflectivity measurements. These biases and corrections are addressed in this work. As the radar has been operational since September of 2018, there is ample data available to diag-nose and to perform the necessary corrections to the system. A variety of methods are employed to validate these corrections including comparing intersecting scan volumes between the UMAXX and nearby WSR-88Ds of the NEXRAD network as well as the use of membership functions.

Key results of this work are:

1. Ground clutter is principally identified through differential phase and secondarily through velocity and co-polar correlation

2. Partial beam blockage is best estimated assuming a 1.67 $^\circ$, 2-way beamwidth with an 8dB cutoff

3. System differential phase and Differential Reflectivity bias are functions of az-imuth due to the radome panels.

4. A linear relation between wet radome attenuation and rain rate is found

5. Using an attenuation factor of a = .28 to determine path integrated attenuation improves correlation of reflectivity measurements between UMAXX and NEXRAD network.

Ultimately, the goal is to establish UMAXX as a reliable and well understood benchmark with which to calibrate Raytheon's dual-polarized phased array radar. The two radars operate in sufficiently close frequencies within X-band and collected data simultaneously while colocated. While phased arrays show great promise and potential in meteorologic observations, they come with many challenges that neces-sitate the use of a trustworthy baseline with which to validate its measurements. Additionally, UMAXX's data is to be streamed to serve as a source to fill any gaps present in the National Weather Service's network in the region.

TABLE OF CONTENTS

LIST OF TABLES

Table	Page

LIST OF FIGURES

CHAPTER 1

INTRODUCTION

The purpose of this undertaking is to prepare and calibrate the UMAXX radar to be used as a reliable and well understood radar to monitor the Pioneer Valley region's meteorological events. The more precisely the UMAXX products are understood, the greater confidence we can place in the studying of meteorological phenomena in the area. Additionally, the mechanically scanned, parabolic dish radar will be used as a baseline with which to validate the design and calibration of Raytheons 2D phased array radar, Skyler, currently on loan to MIRSL. Thus, any uncertainty remaining in UMAXXs calibration will contaminate and perhaps compound in Skyler's measurements.

(a) UMAXX tower from the ground (b) A view inside UMAXX radome

Figure 1.1: UMAXX tower on Orchard Hill

At present, UMAXX (shown in Figure 1.1) is installed in a tower on Orchard Hill in the East-Northeast section of campus and has been in operation collecting weather data since September 19, 2018. The center operating frequency is 9.41 GHz and is transmitted via a 1.2m parabolic dish yielding a 1.85 degree 3-dB beam width in both principle planes. Listed in Table 1.1 are some additional operating characteristics for UMAXX.

Table 1.1: UMAXX Parameters

Center Frequency	9.41 GHz
Peak Power	12.5 kW
Peak Channel Power	6.25 kW
Bandwidth	5 MHz
Polarization	Dual
Beamwidth	1.85 Degrees
Scan Range (azimuth)	360 degrees
Scan Range (elevation)	-5 to 90 degrees
Waveform	Pulse
Sequences	Single, Dual PRT

In 2018, the UMAXX radar (Formerly MA-1) underwent hardware upgrades to support cross polarization measurements [12]. As shown in Figure 1.2, an electromechanical switch was added inline to the vertical transmit channel. This essentially adds in a secondary mode which transmits solely the horizontally polarized channel and receives on both channels; the default mode being Simultaneous Transmit/Simultaneous Receive (STSR). When the UMAXX is in this secondary mode, the vertical portion of the transmit signal is not radiated. Thus, any signal received on the vertical channel should be from cross-polarization leakage present internal or external to the system.

(a) MA-1 Transmit Configuration   (b) UMAXX Upgraded
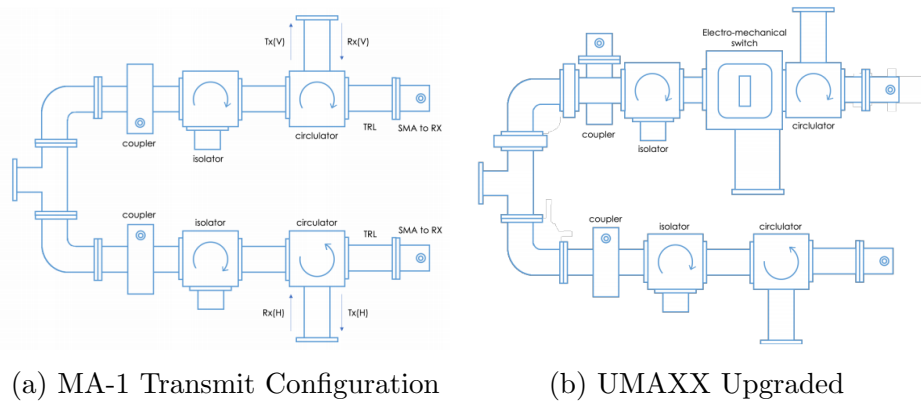
Figure 1.2: MA-1 and UMAXX block diagrams (Image from Sanchez, et al [12])

Chapter 2 introduces a review of various radar products as well as the radar range equation. Having an understanding in this chapter is necessary before reading through the fundamentals of what our calibration goals are and how they will be achieved.

Chapter 3 discusses the issues concerning the complex terrain of the Pioneer Valley. Specifically in the form of clutter present in the data and partial-to-full blockage of the radar's main beam. Non-meteorological reflectors that are observed by the radar are referred to as "clutter". In this chapter, the process of using machine learning to develop a decision tree classifier to identify clutter is explained. Using a 10-fold cross validation, it is shown that it is feasible to construct a classifier with a high rate of detection with an acceptably low rate of false positives (Figure 3.5). Then, to correct for beam blockage, a Digital Elevation Model (DEM) of the region is used in conjunction with a geometric model of the main beam's shape to detect and quantify areas that will partially or fully block the radar's main beam. These results are then compared with observed UMAXX data to derive the effective beamwidth and tune the beam blockage corrections.

Chapter 4 discusses the calibration of Reflectivity Factor and Differential Reflectivity. Reflectivity, particularly at X-band is influenced by the attenuation of heavy precipitation. Many have analyzed the relation between Z and ϕ_{DP}, and have empirically derived linear equations to describe the attenuation to Z using changes in ϕ_{DP} over range ([6], [9], and [10]). A path towards implementing this method is shown here. Then, for the purpose of validating these corrections, a comparison is made against the nearby KENX radar on the NEXRAD network (Figure 4.3). Another source of attenuation is rainfall over the radome which causes a sheet of water to form. This acts as an additional lossy layer the radar signal must propagate through. It has been demonstrated that the presence of water on the radome as well as distant storms will increase the microwave emission incident on the radar (Thompson [11]). Using ϕ_{DP} to calculate the loss of the storm effects of the wet radome, storm, radar,

and atmospheric background are broken out into stages of a cascade to analyze the varying contributions to the radar signal's attenuation. This process yielded a linear relation between rain rate and wet radome attenuation. The results give promise to using the outlined method in conjunction with a stable calibration procedure to mitigate wet radome attenuation.

Differential Reflectivity is also calibrated to account for Differential Attenuation due to heavy rain and any biases that exist internal/external to the system. Differential phase again can be used to correct for differential attenuation due to heavy rain. The UMAXX system itself (including the radome) feature a bias that requires calibration as well. As can be seen in Figure 4.13, differential reflectivity can diverge in azimuth significantly from the expected value. A method is then implemented to mitigate for this bias and removed from the data.

Finally, Chapter 5 draws conclusions on the efforts taken in calibrating this radar and makes suggestions for further actions or improvements that could be explored.

CHAPTER 2

OVERVIEW OF RADAR MEASUREMENTS

2.1 Weather Radar Equation

Before delving into the various data products involved in weather observations, it is worth acknowledging the **Weather Radar Equation**. The Weather Radar Equation is the radars received power, P_{r_0}, related to the collection of individual scatterers within a given scan volume [3]. The relation as given in Doviak and Zrnić [3] is

$$P(r_0) = \frac{P_t g^2 g_s \lambda^2 \eta c \tau \pi \theta_1^2}{(4\pi)^3 r_0^2 l^2 l_r 16 \ln 2} \tag{2.1}$$

where, P_t is the transmitted peak power emitted from the antenna, g is the total antenna gain, g_s is the receiver gain, θ_1 is the antenna's $3dB$ bandwidth, η is the volume reflectivity, λ is the wavelength of the transmitted signal, l is the one-way attenuation of the atmosphere, and l_r is the loss of the matched filter.

Here, Volume Reflectivity η refers to the backscattering cross section per unit volume. When measuring precipitation with short-wavelength (<10 cm) radars as is done here, one can relate the Volume Reflectivity to **Equivalent Reflectivity Factor**, Z_e, by:

$$\eta = \frac{\pi^5}{\lambda^4} |K_w|^2 Z_e \tag{2.2}$$

Where K_w is the complex refractive index of water and Z_e is the Reflectivity Factor which is defined as

$$Z_e = \frac{1}{\Delta V} \sum_i D_i^6 \tag{2.3}$$

Because of Z_e's frequency independence, it is the value most often referred to by meteorologists when discussing the reflectivity of a radar observation. Throughout remainder of this paper, we will simply refer to Z_e as Reflectivity Factor, Z. Rewriting equation 2.1 in terms of Z:

$$P(\boldsymbol{r_0}) = \frac{\pi^3 P_t g^2 g_s \theta_1^2 c\tau \left|K_w\right|^2 Z}{2^{10} \ln 2 \lambda^2 r_0^2 l^2 l_r} \tag{2.4}$$

Note that because the same radar is transmitting and receiving throughout, the radar is assumed stable/consistent and thus P_t g, g_s, θ_1, τ, λ, l, and l_r are taken to be approximately constant. Hence they are combined with the other constants into a variable known as the **Radar Constant**, R_c, to form the following simplified expression:

$$P(\boldsymbol{r_0}) = \frac{R_c Z}{r_0^2} \tag{2.5}$$

2.2   Radar Products

2.2.1   Base Radar Products

Base Radar Products constitute measurements that can be directly obtained from the received signals of the radar. These do not require comparison of two orthogonal polarized signals. They most commonly include **Equivalent Reflectivity Factor**, **Radial Velocity**, and **Spectrum Width**.

2.2.1.1   Reflectivity Factor

Due to its frequency independence (note equation 2.3)The Reflectivity Factor, Z is the preferred way by meterologists to discuss reflectivity [3]. This allows comparisons across different systems which will be leveraged in Section 4.1.2 when the C-Band

NEXRAD network will be used as a reference for UMAXX's X-Band measurements. By rearranging equation 2.5, one can quickly calculate Z by dividing the received power by UMAXXs radar constant and multiply by the square of the range:

$$Z = \frac{P(\boldsymbol{r_0})r_0^2}{R_c} \tag{2.6}$$

Where $P(\boldsymbol{r_0})$ is estimated as follows using the horizontally polarized channel:

$$\overline{S_h} = \frac{1}{M} \sum_{i=1}^{M} |H_{2i}|^2 - \overline{N_h} \tag{2.7}$$

where $\overline{S_h}$ is the mean received power, M is the number of samples, H_{2i} is the received signal of $i^t h$ sample, and $\overline{N_h}$ is the mean noise power. An h in the subscript designates the variable is observed in the *horizontal* channel as opposed to the *vertical* channel which will be indicated by a v in the subscript.

Reflectivity Factor can vary by several orders of magnitude depending upon the severity of rainfall and thus equation 2.6 is typically expressed on a logarithmic scale in units of dBZ:

$$Z(dBZ) = 10 \log Z \tag{2.8}$$

2.2.1.2 Radial Velocity

The UMAXX radar system is a coherent, or Doppler, radar and thus tracks the phase of the received signal. Using the known phase of the received and transmitted signals, the mean radial velocity of the scatterers within a target volume is calculated.

It is important to note that by radial velocity, it implies only the velocity component parallel to the radar beam is captured. There is zero contribution to the Doppler shift from the perpendicular component and thus cannot be deduced by this radar alone.

When receiving successive signals, the phases are compared and deconstructed to approximate the radial velocity component. The phase will be of the form

$$\phi = \frac{-4\pi}{\lambda} v_r \Delta t \tag{2.9}$$

Where ϕ is the phase, v_r is velocity, and Δt is the PRT or $\frac{1}{PRF}$. The radial velocity recorded is in fact an average of the samples received during the dwell along that radial.

2.2.1.3 Spectrum Width

Spectrum width essentially provides the range of velocities within a given range bin. When factors such as turbulence and wind sheer occur within a range bin, the range of Doppler shifts will be wide thus producing a large spectrum width. It can also be thought of as standard deviation of velocity.

As demonstrated in [3], spectrum width is typically derived from estimated auto-correlation function $\hat{R}(T_s)$ and signal power estimate $\hat{S}$

$$\hat{\sigma}_v = \frac{\lambda}{2\pi T_s \sqrt{2}} \left| \ln \left(\frac{\hat{S}}{\left| \hat{R}_1 \right|} \right) \right|^{\frac{1}{2}} \tag{2.10}$$

Where T_s is simply the pulse repetition time.

$\hat{R}_1$ with sample time lag time T_s can be approximated as

$$\hat{R}(T_s) = \frac{1}{M} \sum_{m=0}^{M-1} V^*(m) V(m+1) \tag{2.11}$$

and for $\hat{S}$ we have

$$\hat{S} = \frac{1}{M} \sum_{k=0}^{M-1} |V(k)|^2 - N \tag{2.12}$$

These operations are done for both polarization channels and to approximate the true spectrum width the average is taken between the two results.

2.2.2 Dual-polarization Products

2.2.2.1 Differential Reflectivity

Differential Reflectivity, or ZDR, is a crucial product yielded from the dual polarizations. Essentially ZDR is a ratio between the received horizontal and vertical mean sampled powers. Given error reflectivities less than .2 dB, it is possible to gain a higher level of accuracy when measuring rainfall quantities than when using Reflectivity alone (Ventura et al) [6]. To obtain ZDR, $\overline{S_h}$ and $\overline{S_v}$ are calculated directly over M samples as was done for volume reflectivity in equation 2.2. We have [3]:

$$\overline{S_h} = \frac{1}{M} \sum_{i=1}^{M} |H_{2i}|^2 - \overline{N_h}, \tag{2.13}$$

$$\overline{S_v} = \frac{1}{M} \sum_{i=1}^{M} |V_{2i+1}|^2 - \overline{N_v} \tag{2.14}$$

Where $\overline{S_h}$ and $\overline{S_v}$] are the mean sampled horizontal and vertical powers, H and V are the received horizontal and vertical samples, and $\overline{N_h}$ and $\overline{N_v}$ are the mean sampled noise powers.

The i-subscripts indicate position in time; however, note that because UMAXX's default mode is STSR, the samples are not interwoven but in fact recorded at the same time step. This has the added benefit of twice as many samples for a given dwell time. Thus,

$$\overline{S_h} = \frac{1}{M} \sum_{i=1}^{M} |H_i|^2 - \overline{N_h}, \qquad (2.15)$$

$$\overline{S_v} = \frac{1}{M} \sum_{i=1}^{M} |V_i|^2 - \overline{N_v} \qquad (2.16)$$

and

$$\overline{Z_{DR}} \equiv 10 \log \frac{\overline{S_h}}{\overline{S_v}} (dB) \qquad (2.17)$$

2.2.2.2 Propagation Differential Phase

Propagation Differential Phase, or ϕ_{DP}, is the measure of the difference in phase of the horizontal and vertical polarizations due to a delta in the electrical length of the propagation paths of the two polarization channels. With a little effort, ϕ_{DP} can be extracted from the UMAXX's *observed* differential phase, Ψ_{DP}. In addition to effects due to the waves' propagation paths, Ψ_{DP} will feature a system differential phase, ϕ_0 and a potential backscatter ϕ_{BS}.

System differential phase, ϕ_0, is the baseline difference in phase between the two polarization channels due to differing electrical lengths internal to the transmit and receive pathways. This value is relatively stable and can be determined by analyzing the first range bins along a radial to encounter a patch of dense rain fall. This initial value obtained along the radial has had little opportunity to drift and is close to the true ϕ_0. For this thesis, many sample bins were averaged in an attempt to best approximate the ϕ_0. This averaged value is then subtracted from Ψ_{DP} to obtain ϕ_{DP}.

Backscatter differential phase, $\phi_{DP,bs}$, occurs with larger, more complexly shaped scatterers. They are the result of resonance effects when the scatterer is not small compared with the wavelength such as large hail or wet snow. In general, for rain, this portion of the measured ϕ_{DP} is considered small ($< 1.5 \deg$) [3].

11

Propagation differential phase, ϕ_{DP}, is the portion of Ψ_{DP} of primary concern in this thesis. In the case of nearly symmetrical (spherical) scatterers, there will be very little difference in the paths of the two polarization channels and thus this value will drift minimally. In an event such as heavy rain, the hydrometers are oblate spheres and larger in the horizontal polarization than the vertical. The two polarization channels' paths of propagation will be of unequal electrical lengths as the horizontal channel encounters a greater percentage of the hydrometeors than the vertical channel. Due to this imbalance, the ϕ_{DP} trends positively.

$$\phi_{DP} = \phi_H - \phi_V \qquad (2.18)$$

Where ϕ_H and ϕ_V are the horizontal and vertical channels' phase, respectively. Since the measurement is strictly a phase quantity, it is unaffected by factors such as attenuation, partial beam blockage, or radar miscalibration [7]. As such, it is a useful tool in correcting for attenuation in severe weather.

2.2.2.3 Co-polar Correlation Coefficient

Co-polar Correlation Coefficient, or ρ_{HV}, is a measure (from 0 to 1) of how correlated the two polarization channels behave from pulse to pulse [Kumjian] [7]. This serves as an indication of how diverse the geometric shapes of the scatterers are in a given volume. Smooth, nearly spherical drops (light rain) will contribute equally to changes in either channel, thus a correlation coefficient $> .98$ is expected. Pure dry hail behaves similarly but when wet can produce values $< .95$. Ground clutter and chaff are much more complexly shaped and will produce values $< .8$ [7]. As will be seen later, this distinction will play a role in identifying and removing clutter from the radar scans. The magnitude of the Copolar Correlation Coefficient can be defined [2] as

$$|\rho_{co}| = \frac{|\langle n\left(S_{hh}S_{vv}^{*}\right)\rangle|}{\sqrt{\langle n\left|S_{hh}\right|^{2}\rangle\langle n\left|S_{vv}\right|^{2}\rangle}} \qquad (2.19)$$

Where S_{hh} and S_{vv} are the received scattered powers for the H- and V-channel, respectively.

CHAPTER 3

CLUTTER CLASSIFICATION AND BEAM BLOCKAGE CORRECTION

3.1   Ground Clutter Filter

Ground clutter arises from obstructions in the landscape both natural and man-made that interfere with the radar's observations. This occurs either via partial/total blockage of the main beam, or reflections from the antenna side lobes. With a coherent, dual-polarized radar, there exists several data products that make it possible to discern between reflections from clutter and weather phenomena. Ground clutter, for example, should have near zero radial velocity. Second, ground clutter is much more complex in shape than hydrometeors and thus will give seemingly random, or noisy ZDR values. For this same reason, there will be very little correlation between the two channels. As explained in section 2.2.2.3, the co-polar correlation coefficient is predicted to be $< .8$ for non-hydrometeors.

3.1.1   Present Filter

Presently, we have a crude filter in place to remove clutter. Essentially any range bin with a sufficient signal to noise ratio that has $\rho_{HV} < .6$ is presumed ground clutter and ignored. Raising this level of ρ_{HV} any further without proper precautions may also increase the rate of false negatives - leading to the unintended omission of weather data. Additionally, the mean of the samples in a given dwell period are subtracted from the data. The reasoning here is it is assumed that when observing weather, the samples of a dwell period will have a complex mean of zero. Any amount the mean drifts from zero is likely due to contributions from stationary ground clutter.

3.1.2 Decision Tree Classifier
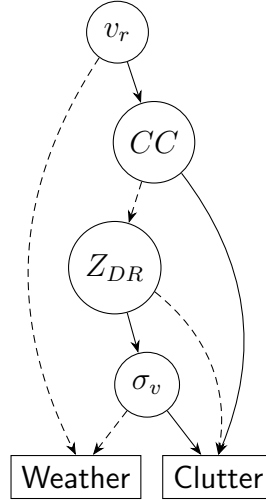
Figure 3.1: General Structure of potential binary tree

By utilizing machine learning, we can comb through high volumes of pre-classified data to find the optimum cut-off point for parameters such as ρ_{HV} and Z_{DR} unique to this radar. Using scikit-learn, a Python machine learning package, UMAXX data was analyzed in this expanded variable space and a more precise and definitive boundary between clutter and weather was implemented. In the past, decision trees have been used in weather radar post-processing to decide if a given range bin is predominantly filled with clutter or precipitation [8]. The data algorithm also lends itself well to machine learning techniques and is utilized frequently. The goal is by creating the classifier based around previously collected UMAXX data (training data), system-specific boundaries are derived that maximize clutter detection while simultaneously attempting to minimize false negative detections.

3.1.2.1 Training the Model

To train our model, we first established a preclassified training dataset. This can be done simply by identifying days in which no weather occurred and classifying all range bins as ground clutter. Then, identify days with which there is weather

and classify all populated range bins sufficiently distant from the radar ($\approx 30km$) as weather. It is also important here to utilize different days with varying instances of weather to ensure we get enough variation in data and don't specialize our filter too closely with a particular day.
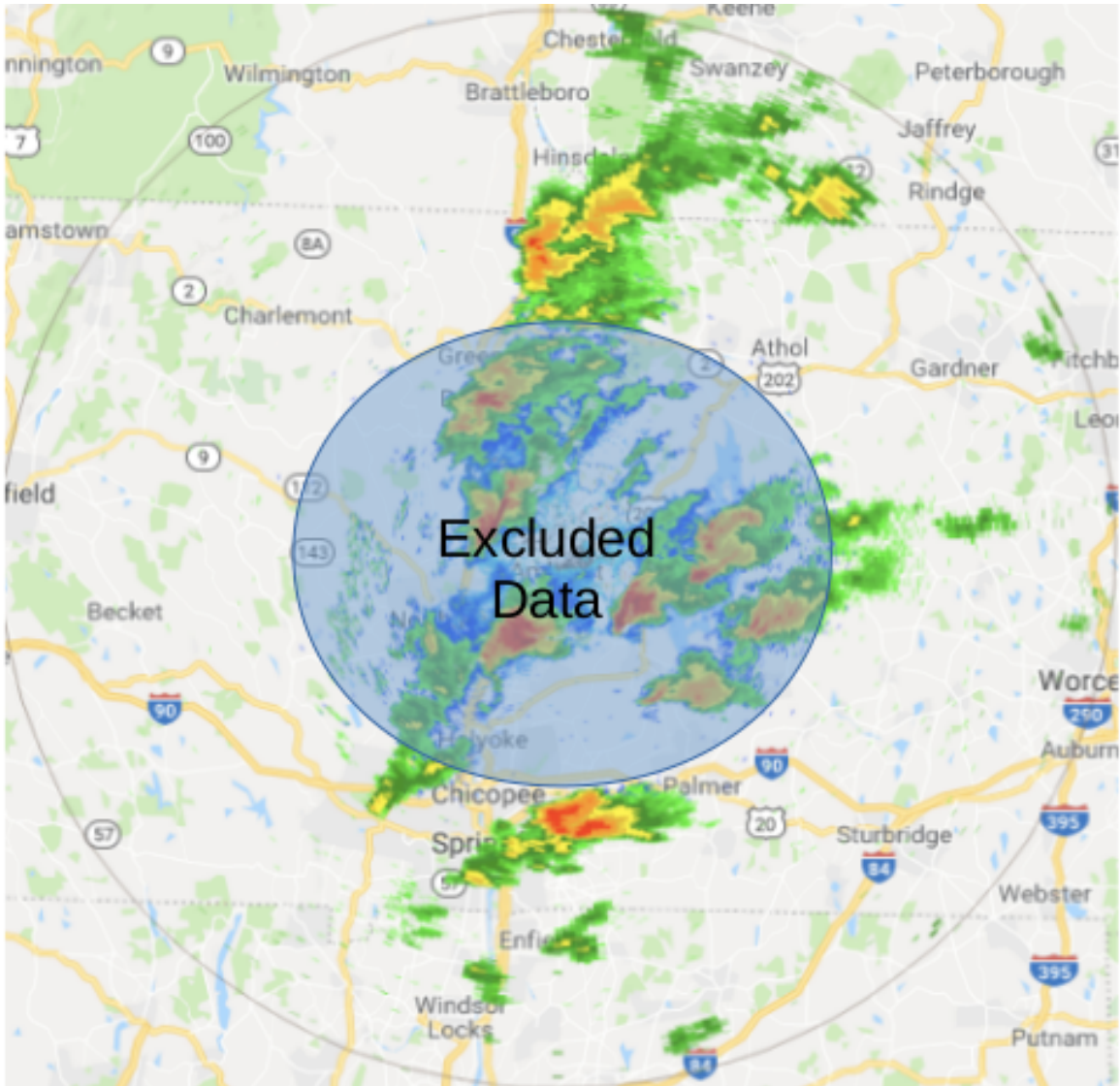
Figure 3.2: Shows an example storm with data excluded close to radar. Although large amounts of data are unfortunately removed in the process, there are substantial days of data collection during storm events to provide more than enough data to work with.

Once the dataset is established, one can observe how the clutter and weather data behaves differently when looked at through the various observables as shown in Figure 3.3.

Certain products are more telling than others. Ψ_{DP} for example is centered close to -160 degrees for weather due to that being the approximate ϕ_0 location (see section 4.1.1.1). Conversely, clutter has a more uniformly random distribution. Note there is spike at 0 degrees, likely due to cross polarization that results in comparing the phase of a channel with itself.
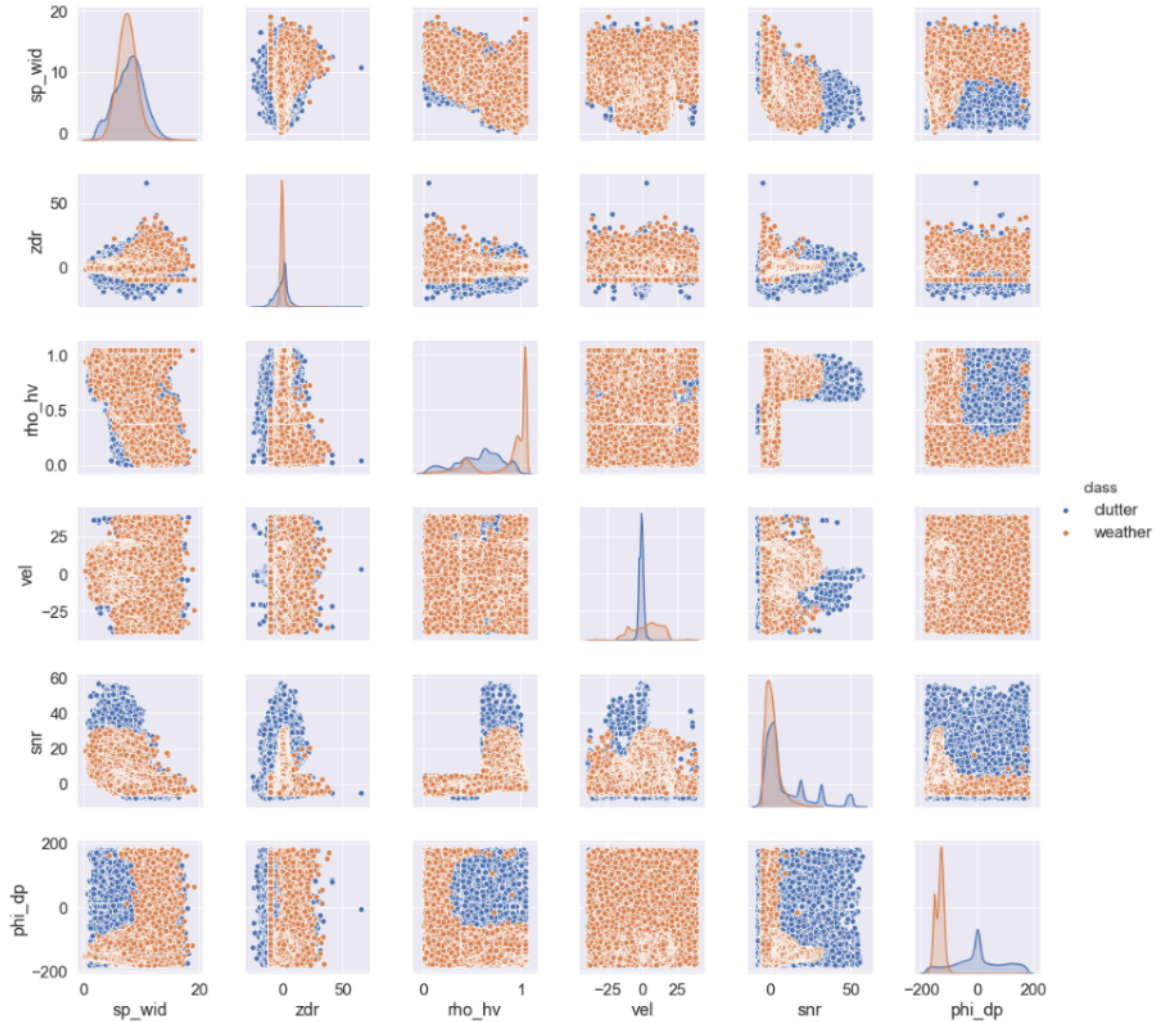
Figure 3.3: X and Y axes are various radar products to be plotted against each other. Along diagonal is a kernel density function approximating the probability distribution of clutter and weather data points for that particular product. Off diagonal shows scatter plots of two radar products.

The tree is then constructed using an algorithm that prioritizes maximum entropy. In this context, maximum entropy is determined by choosing an observable and a threshold which best separates the two classes of data (clutter and weather). The algorithm proceeds in this way until it reaches either a preset level of purity at a particular node (or leaf), or a preset depth of decisions. Both the purity and depth are empirically determined and are chosen to best balance accuracy of the classifier as well as complexity, which directly impacts latency.
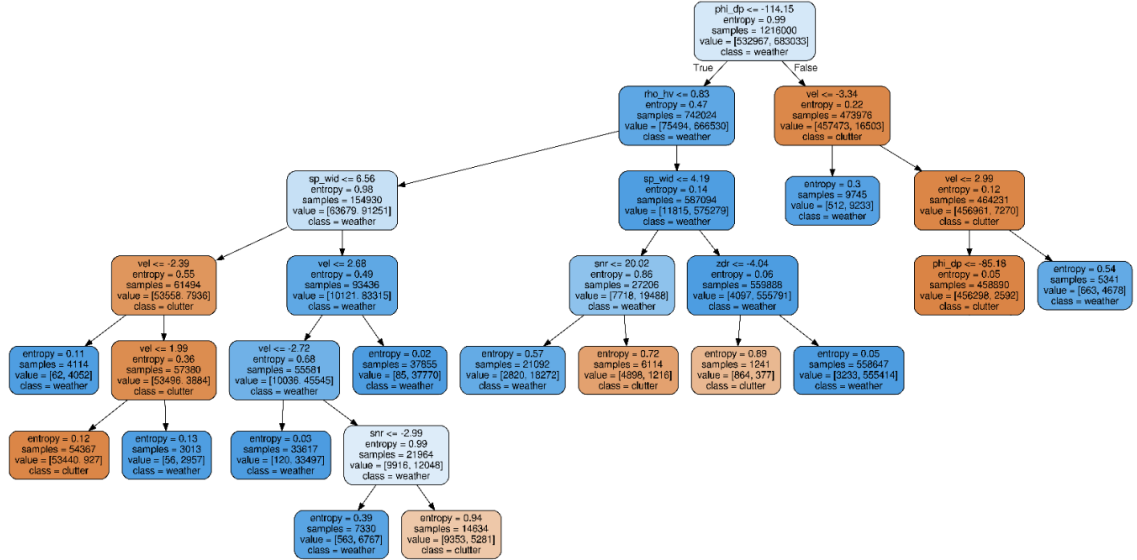
Figure 3.4: This figure shows a graphical representation of the resulting decision tree generated by the scikit-learn's classifier package. The top line on the node states the parameter and threshold of the decision. The second line states the **entropy** of the node, or how well mixed the sample set is. The closer to 0, the more uniform the node is. Then there is sample size, distribution of samples, and majority classification (weather or clutter)

In Figure 3.4, one can track how the classifier makes its decisions. Each node represents the algorithm selecting the measurement and its threshold based on the greatest reduction in entropy. The nodes which reveal the most insight and confirmation into the nature of the targets being observed are as follows: the most significant separator of clutter and weather bins is the ϕ_{DP} value with a threshold of -114.15 degrees. The tree implies that range bins above this threshold are largely clutter. The significance of this threshold value will be made clear in sec 4.1.1.1 when ϕ_0 is determined. For values above this threshold, radial velocity is check: if close to 0 $(-3 < v_r < 3)$, then range bin is deemed likely to be clutter. For range bins below the ϕ_{DP} threshold, $\rho_{HV} < .83$ is checked. Values less than this indicate the targets in the range bin have less correlation in the horizontal and vertical channels than to be expected for rainfall.

Beyond these primary levels in the decision tree, range bins are checked for conditions such as a narrow spectrum width ($\hat{\sigma}_v < 6$) and larger negative Z_{DR} ($Z_{DR} < -4$). Range bins with values agreeing to these conditions are less likely to be weather and thus omitted from the final data.

The resulting tree shown in Figure 3.4 can easily be implemented in the format of a series of $if...else$ statements as follows:

```
for each bin in range_bins:
  if (bin.phidp <= -114.15):
    if (bin.rho_hv <= 0.83):
      if (bin.spec_width <= 6.56):
        if (-2.39 <= bin.vel <= 1.99):
          bin.setClass('clutter')
        else:
          bin.setClass('weather')
      else: //bins with spec_width > 6.56 very likely to not be stationary clutter
        if (-2.72 <= bin.vel <= 2.68):
          if (bin.snr <= -2.99):
            bin.setClass('clutter')
          else:
            bin.setClass('weather')
        else:
          bin.setClass('weather')
    else if (bin.spec_width <= 4.19): //cross corr larger than .86 is largely indi
      if (bin.snr <= 20.02):
        bin.setClass('weather')
      else:
        bin.setClass('clutter')
```

```
    else if (bin.zdr <= -4.04):

      bin.setClass('clutter')

    else:

      bin.setClass('weather')

  else if (-3.34 <= bin.vel <= 2.99):

    bin.setClass('weather')

  else: //near-zero velocity bin with phi_dp greater than -114 deg

    bin.setClass('clutter')
```

3.1.2.2 Verification

Once the tree had been constructed, it was validated by generating a Receiver Operator Characteristic Plot. This was done by using a 10-fold verification algorithm. essentially a rotating 9/10's of the data builds the tree while the remaining 1/10 validates the thresholds. This is done 10 times to build confidence/enforce the validity of the decision tree. Figure 3.5 shows the classifier produces a ROC that approximates an ideal right angle.
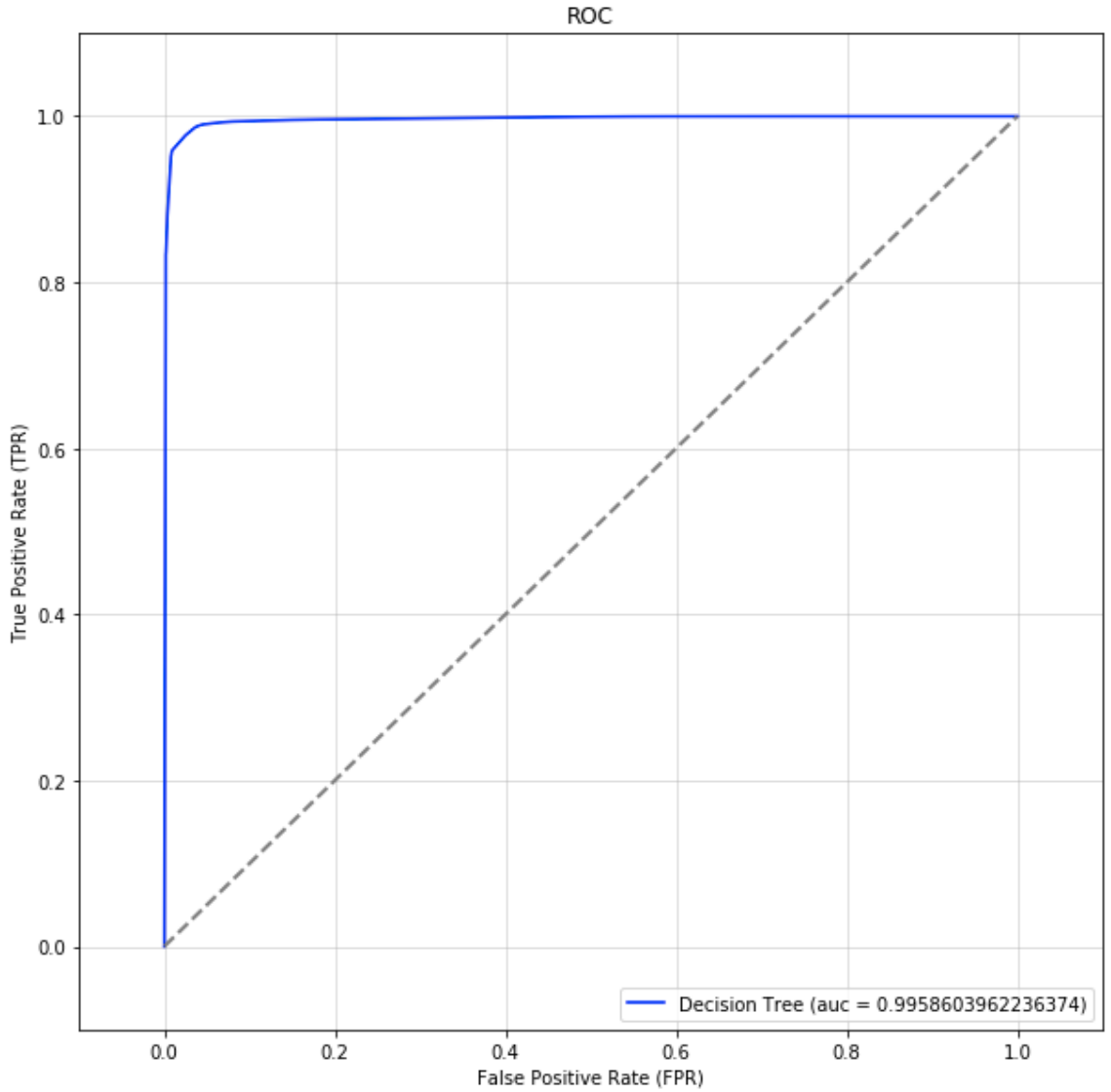
Figure 3.5: ROC Plot: This receiver operating characteristic plot seeks to demonstrate the accuracy with which the decision tree can distinguish clutter from weather

Figures 3.6 and 3.7 demonstrate the application of the decision tree in classifying real data. The clear day plot (3.6) is an example at 1 degree tilt when zero filtering is applied (all clutter was left in). The latter (3.7) shows the difference between our current, crude filter and the decision tree classifier in the presence of precipitation.
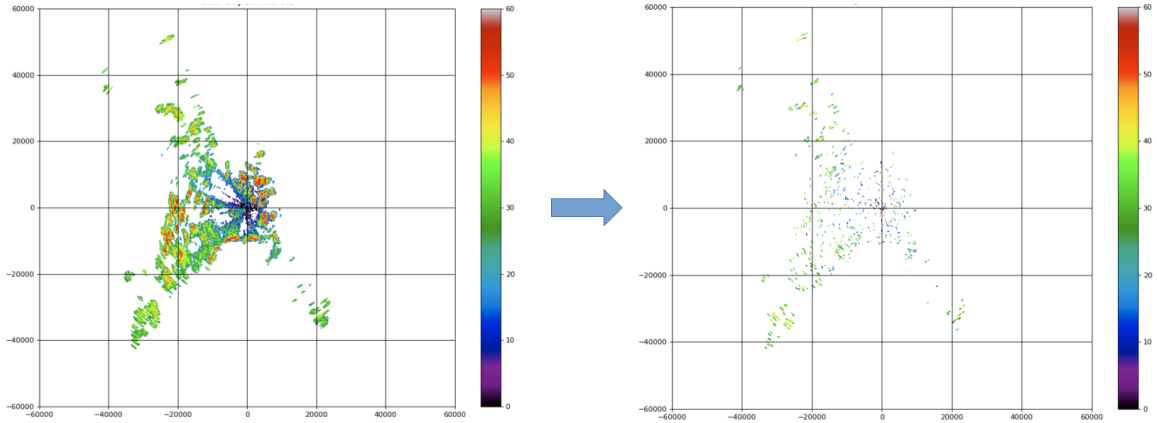
Figure 3.6: **Clutter Filtering on a Clear Day**: This example features no filtering whatsoever at a 1 deg tilt. Here it can be seen how severely the radar scrapes along the terrain. In the right, after applying the clutter classifier, we see that a very large percentage of the clutter has been removed.
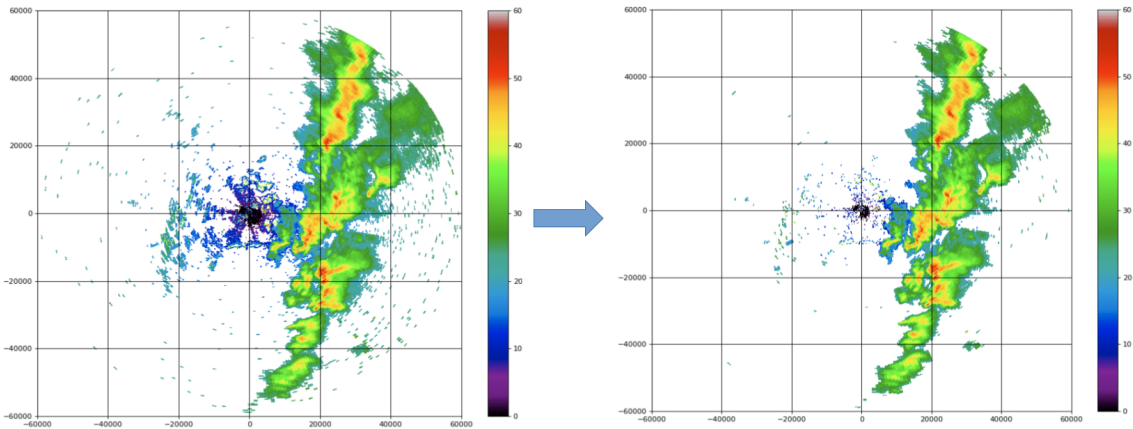
Figure 3.7: **Clutter Filtering on a Stormy Day**: This example features a storm and the crude clutter filter mentioned in Section 3.1.1. Notice here that again a large percentage of clutter is removed, yet storm system is intact. This highlights the improvements made from present crude filter to the decision tree classifier.

3.2   Partial Beam Blockage Correction

In addition to obscuring data in the form of clutter, complex terrain can also block significant portions of the radar's main beam. Since the receiver has no way of "knowing" this, the data will under report any precipitation that may exist further

along the radial beyond the point of blockage. The resulting effect will be regions of stepped-down reflectivity levels that will appear as shadow-like cones emanating outward from the regions of blockage. This section explains the process by which a Digital Elevation Model of the region was used as well as an approximation of the energy distribution of the radar's main beam to analyze the effects of partial beam blockage and attempt to correct for them.

3.2.1   Digital Elevation Model

By using a digital elevation model (DEM), one can calculate the angle of approach to surrounding obstructions and eventually the percentage of beam blockage by approximating the main beam as a first-order Bessel function. Figure 3.8 shows the angle of approach (in degrees) from the UMAXX location to the point in the terrain.
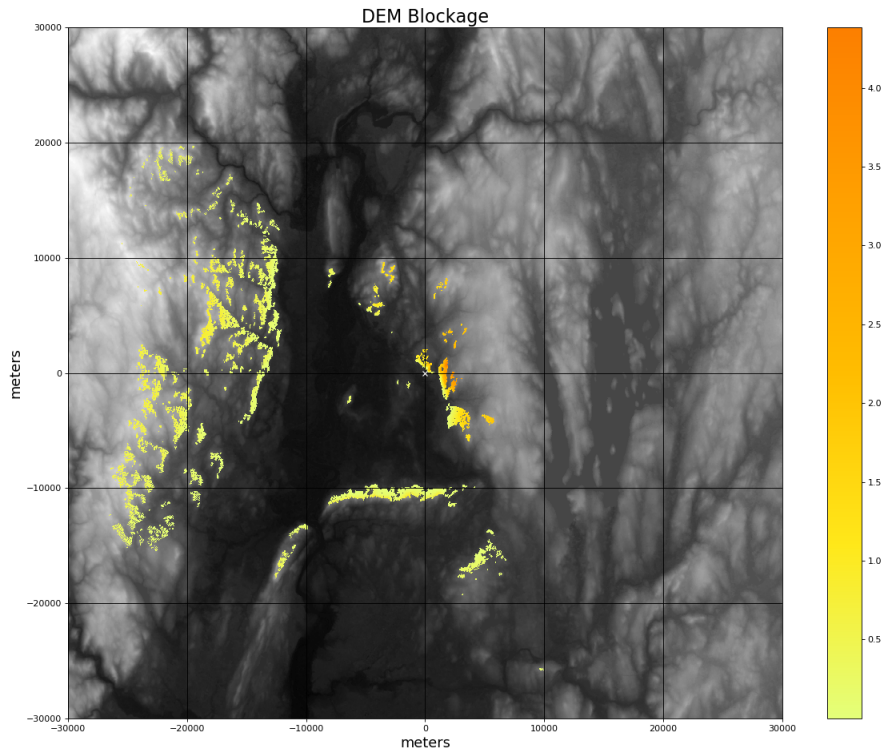
Figure 3.8: Location and level of UMAXX beam blockage overlaying Digital Elevation Model: With UMAXX located at center, highlighted regions are points which could potentially block the main beam. The colorbar conveys what degree tilt from radar objects are blocking.

After processing the DEM with UMAXX's beam characteristics as presented in Figure 3.8, a mapping is generated to translate the radar beam's azimuthal direction and range into a level of blockage with respect to tilt angle as shown in Figure 3.9. It's important to note these levels of blockage are only increasing with distance. For example, along a given radial at a particular range bin, if the main beam is obscured below 1 degree angle of approach from the UMAXX location, then the beam will be blocked by at least that degree for further range bins and increase as it reaches taller obstacles.
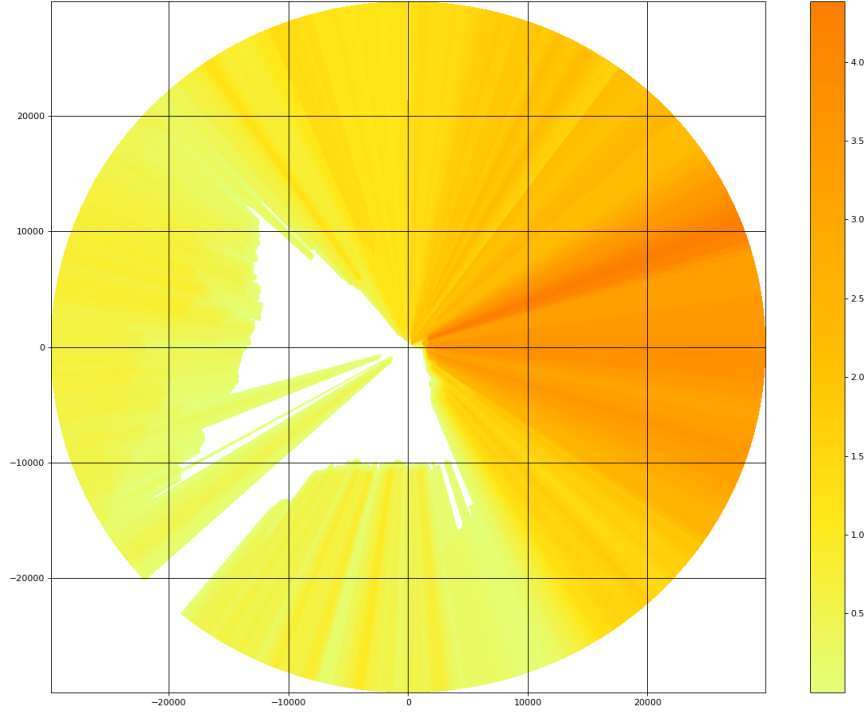
Figure 3.9: Levels of Beam Blockage: Using findings from Figure 3.8, radials track maximum blockage moving away from center. Everything below tilt shown in colorbar will be obscured by terrain.

3.2.2 Beam Shape

To determine beam shape for a parabolic reflector antenna, there are well documented formulas that describe the shape of radiation intensity for an ideal reflector antenna ([1] and [13]). Below are the formulas that represent the θ and ϕ (in context of spherical coordinates) components of the Electric Field.

$$E_{\theta s} = \frac{jke^{-jkr}}{4\pi r}(1 - \cos\theta) \int\int_{S_0} (-E_{ax}cos\phi - E_{ay}sin\phi) \times e^{jk(x'\sin\theta\cos\phi + y'\sin\theta\sin\phi)}dx'dy'$$

(3.1)

26

$$E_{\phi s} = \frac{jke^{-jkr}}{4\pi r}(1-\cos\theta)\int\int_{S_0}(-E_{ax}\sin\phi + E_{ay}\cos\phi) \times e^{jk(x'\sin\theta\cos\phi + y'\sin\theta\sin\phi)}dx'dy'$$

(3.2)

where, $E_{\theta s}$ and $E_{\phi s}$ are the θ and ϕ components of the transmitted E-field, k is the wave number, r is the range to an observation point, S_0 is the projected cross-sectional area, x', y' are positional vectors on the surface S_0, and θ, ϕ are the angle of sight line to observation point in relation to the center of surface S_0.

Using the equations for the E-fields of a parabolic reflector antenna, a model for the shape of the beam is developed and used to determine percentage of beam blockage at any given tilt, azimuth, and range.

When determining the beamshape of a reflector antenna, the projected, two dimensional shape of the broadside of the antenna is approximated as the radiating element [1]. In the case of UMAXX, this is taken to be a flat circle of radius 1.2m. Using the symmetry available due to this fact, Equations 3.1 and 3.2 reduce to simply

$$E(\theta) = 2\pi r_0^2 \frac{J_1(\xi)}{\xi}$$

(3.3)

where $\xi = 2\pi\frac{r_0}{\lambda}\sin\theta$ and $J_1(\xi)$ is the first order Bessel function. This drastically simplifies the analysis of the antenna's beam shape and can readily be solved to determine our radiation pattern as shown
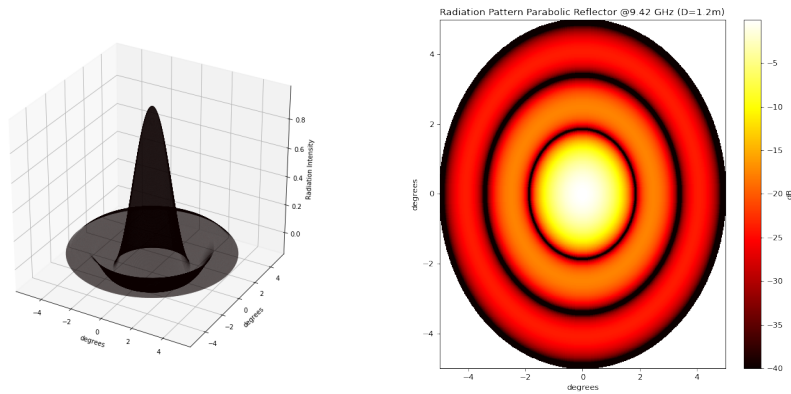
(a) 3D Model of the radiation intensity of UMAXX antenna

(b) Radiation intensity in dB. x- and y-axis represent degrees off from boresight.

With a model of radiation intensity established, it is now possible to utilize the blockage progression derived in Sec 3.2.1 to solve for the percent of energy blocked during transmit/receive through UMAXX's scan strategy. The method is essentially to sweep outward along each radial and track the maxima in the terrain as the beam moves outward from the radar. At each successive range bin the area under the current maxima will be summed and taken to be the portion of blocked energy. Divide this by the total area under the radiation pattern's main beam and the result is percentage of the energy blocked.

3.2.3 Generating Blockage Correction Tables

So with the blockage progression along each radial defined and an approximation of the main beam available, it is possible to attempt to determine the percentage of energy blocked at each range bin along a given radial. A 2D integration is performed between the current maximum along a particular radial and the beam's radiation pattern to determine the percentage of transmitted energy that is obscured by the terrain. This is done for each tilt angle as shown in Figure 3.11. This beam blockage

28

percentage is then converted to a loss value in dB to be added to the reflectivity, Z, to compensate for the blocked portion of the beam.
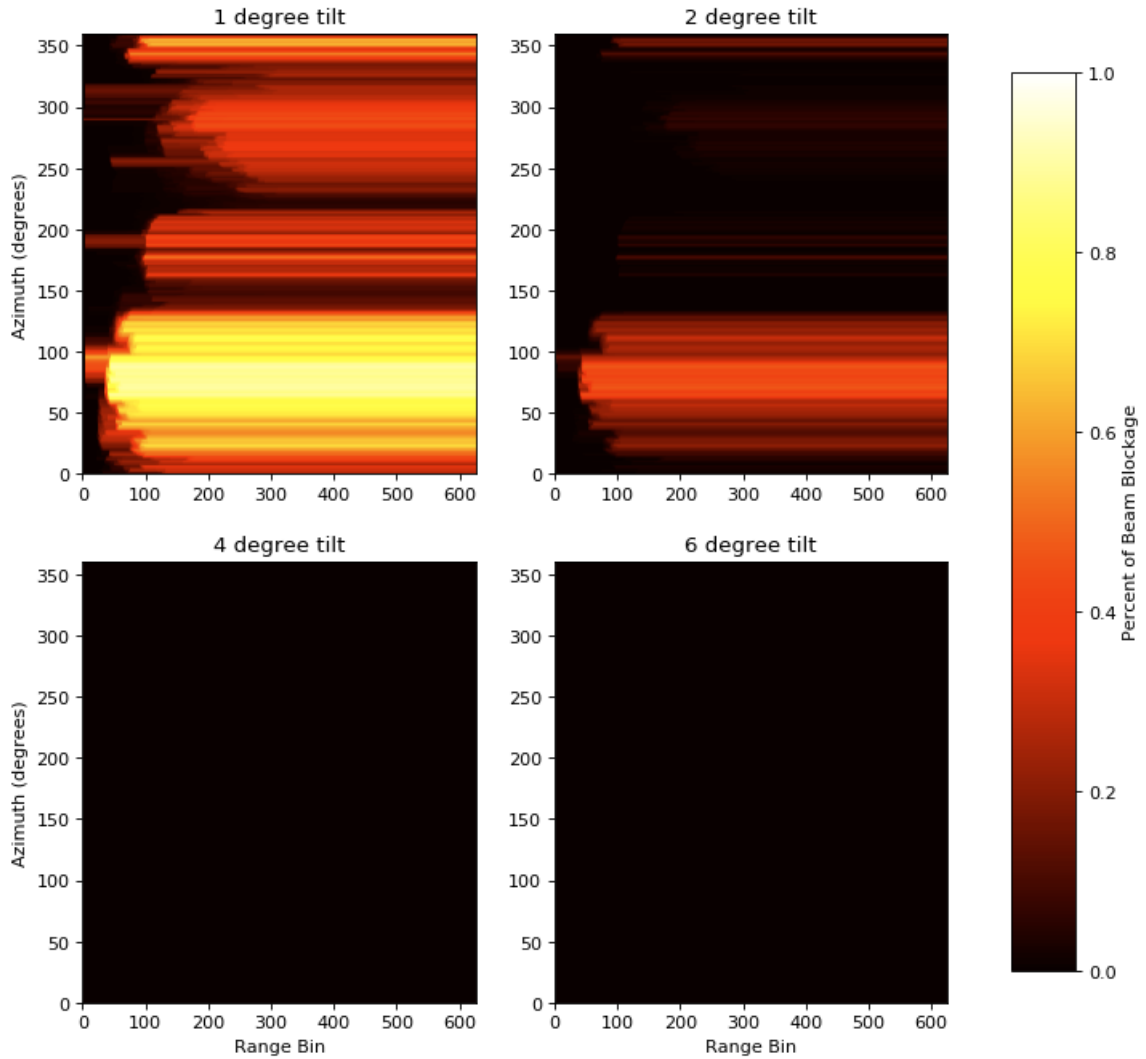
Figure 3.11: Blockage Correction Tables (by tilt): 1 degree tilt experiences some level of blockage in nearly every direction. 2 degrees still sees blockage due to Pelham Hills to the east. 4 and 6 degree tilt observe near zero blockage.

3.2.4 Validation Using Averaging by Scan Angle

Next, it is crucial to compare our model of UMAXX's blockage levels with actual reflectivity factor data in order to validate our correction tables. The results presented in the previous section represent the beam blockage that would be expected if the

UMAXX system possessed the sensitivity to capture the entire main beam within the first null. However it is unlikely for any system to have this level of sensitivity, thus real data is needed to determine the *effective beam width*.

To do so, the average of several rain events at each tilt angle were calculated. During data collection, the various tilt angles are interleaved and thus adjacent tilt angles should see very similar results on average in an environment containing zero blockage. Any delta that exists between tilt angles can thus be attributed to blockage due to terrain.

This delta is then compared against the delta of the correction tables determined via the DEM. A non-unity correlation implies the beam width in the blockage progression model needs to be adjusted. In doing so, this has the added benefit of experimentally determining the effective beam width of the radar. This is necessary because our receiver is lacking the sensitivity to detect the entire beam width out to the first null. As such, it would yield misleading results to consider that entire region of the beam when calculating the percentage of energy obscured by the terrain.

To find the effective beam width, start with the entire main beam and incrementally contract narrower until the regression line relating the DEM correction table to the averaged data has a slope of 1. For this radar, an 8-dB cut-off point resulting in a 1.67 degree, 2-way beam width is sufficient.
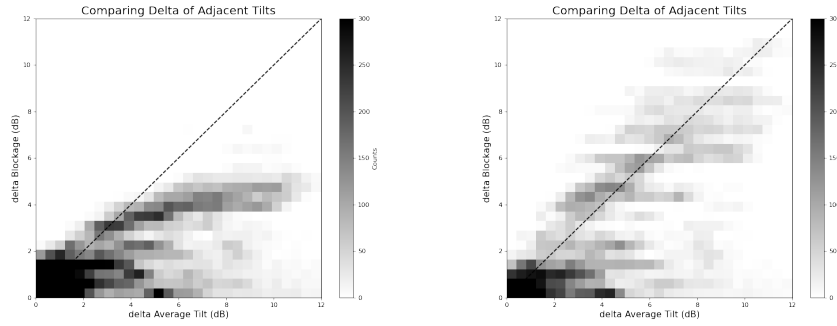
(a) Comparison w/ Full Beam   (b) Comparison w/ Effective Beam

Figure 3.12: A comparison of the calculated beam blockage corrections and averaged Z data. A 2D histogram of deltas for the point pairs are plotted on a logarithmic scale. Point pairs are determined based on coinciding azimuth and range bin. Here one can see the improvement when using the determined effective beam width of the UMAXX Radar. By adjusting the effective beam width we are able to calibrate DEM blockage correction table to represent the true levels of blockage that the UMAXX radar is seeing.

With the beam blockage table calibrated against averaged data, the corrections can be applied to an actual data frame. in Fig 3.13, UMAXX is looking at a storm passing to its north using the 1 degree tilt angle. After applying the corrections in (b), one can see an improvement to the shadows as well as an overall increase in the region. This is due to partial obscurity in nearly all directions when using the 1 degree tilt as can be recalled after referring to Fig 3.11.

(a) Uncorrected UMAXX Data   (b) UMAXX Data Corrected
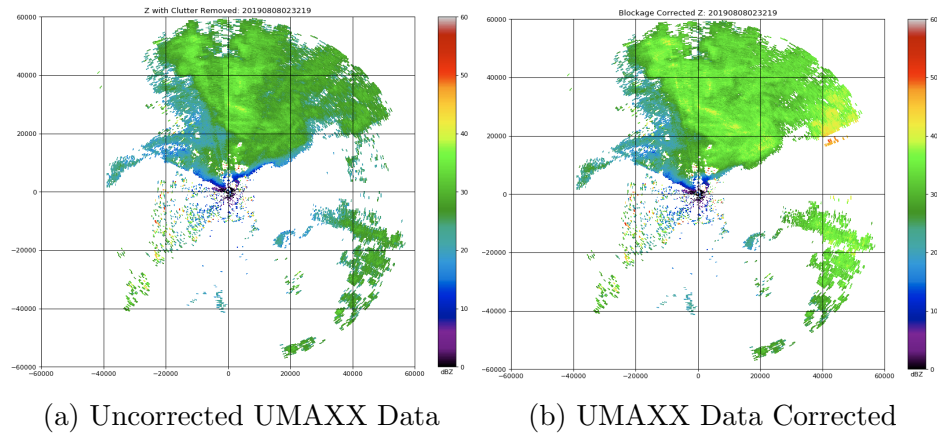
Figure 3.13: Here is the data displayed at 1 deg tilt and with obvious blockage (note the shadows cast in left image). After applying beam blockage corrections, we can see the shadow-effect is mitigated and an overall higher intensity of reflectivity.

Below in Figure 3.14 is another example featuring a significant amount of blockage to the east at a 2 degree tilt. This sector is normally completely blocked at the 1 degree tilt, but at 2 degrees still is at least partially recoverable.
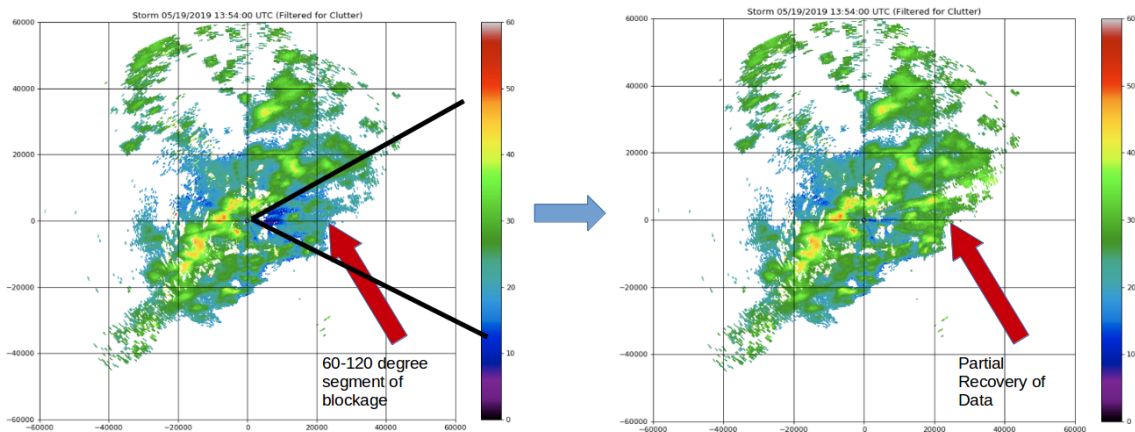
Figure 3.14: Significant blockage is corrected at a 2 degree tilt due to shadowing by the Pelham Hills.

CHAPTER 4

REFLECTIVITY AND DIFFERENTIAL REFLECTIVITY CALIBRATION

4.1   Reflectivity Factor Calibration

There are two sources of attenuation impacting reflectivity factor measurements that will be addressed in this section. First, is the two-way path integrated attenuation (PIA). This is the attenuation that the radar signal experiences as it propagates to the scatterer and reflects back to the radar. At X-band, this effect is more severe than at lower frequencies and needs to be addressed. For this, many have examined the relation between ϕ_{DP} and attenuation ([5], [6], and [9]). These works have resulted in an attenuation factor that can be used to approximate levels of attenuation using ϕ_{DP}. This chapter will further study and verify those findings as they apply to UMAXX. The results after applying these attenuation corrects, in addition to the beam blockage corrections, will be validated using the Albany NEXRAD radar KENX.

Another issue that needs attention is the variation in radome attenuation UMAXX sees when the radome is wet or dry. The presence of water on the radome results in a warmer scene from perspective of the antenna. This increase in brightness temperature is visible when viewing the noise floor. Efforts have been made to relate this increase in temperature to a radome attenuation ([11]) and will be investigated in this chapter as well. In an attempt to verify this method, the KENX radar site will again be leveraged as a baseline data set for comparison.

4.1.1 Path Integrated Attenuation Correction Using ϕ_{DP}

The linear equation for correcting PIA is as follows:

$$Z_e^{int} = Z_e + a\phi_{DP} \qquad (4.1)$$

where, Z_e^{int} is the intrinsic (true) reflectivity factor, Z_e is the reflectivity observed by UMAXX, ϕ_{DP} is the differential phase of the echo, and a is the attenuation coefficient used to scale ϕ_{DP} to an attenuation value.

The key here is the attenuation coefficient, a. It scales the changing ϕ_{DP} value to compensate for the attenuation the propagating wave was subjected to along that radial. Generally the accepted value to use is about .28 ([9]) and is the value to be used throughout the analysis in this paper.

4.1.1.1 System Differential Phase, $\phi_{DP,sys}$

Before the horizontal and vertically polarized waves emit from the radar, they are subject to a variation in phase due to the difference in their respective path lengths. This initial difference is known as the System Differential Phase, ϕ_0. Since the PIA calculation proposed relies on calculating the difference in phase between these two channels, it is necessary to determine this system bias and remove it from the measurement.

$$\phi_{DP} = \Psi_{DP} - \phi_0 \qquad (4.2)$$

This can be done simply by observing various rain events over long periods of time and averaging the earliest echoes along each radial. The idea here is that through open air the phase between the two channels should not diverge, thus upon first contact with rainfall the Ψ_{DP} of the first received echoes should be largely attributed to the system bias. Once this value is determined, it can be subtracted from the measured differential phase Ψ_{DP} to determine true ϕ_{DP}. The resulting data is displayed in Fig

(4.1). One can see in the figure that aside from the anomaly in 1 degree tilt, the variation is approximately 8 degrees which amounts to a swing of ≈ 2.24 dB thus highlighting the necessity to consider azimuth before performing corrections.
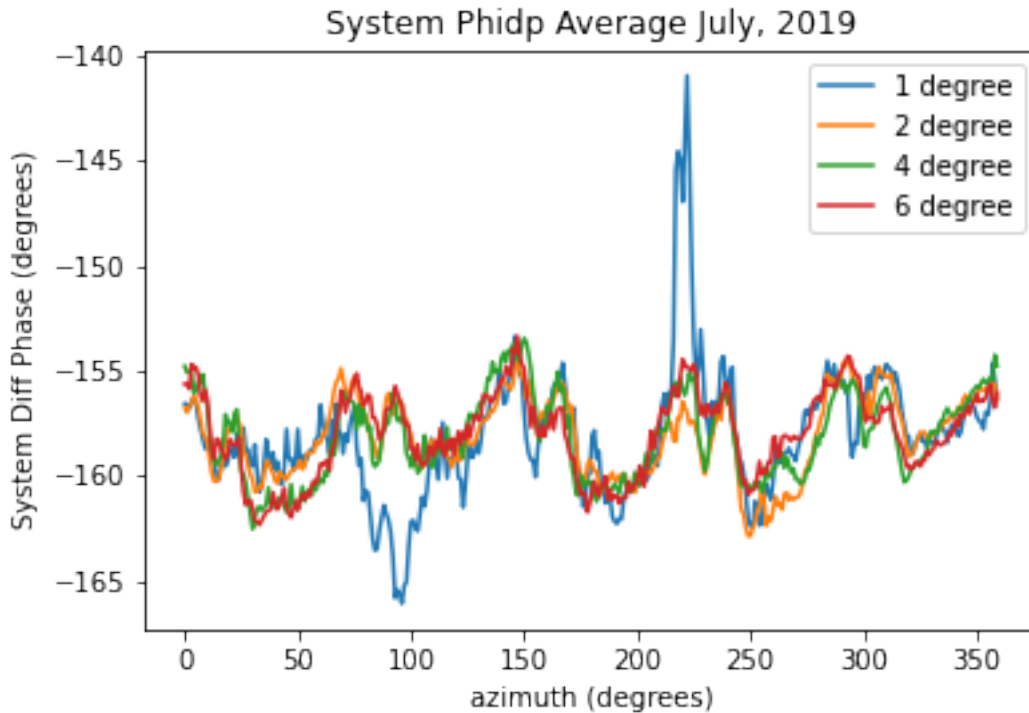
Figure 4.1: Plotted above are the ϕ_0 values calculated for each tilt angle: Note the azimuth dependence. Can make out 5 peaks which correspond well with 5 panels that make up the radome. the 1 degree tilt has some variance in it likely due to the heavy level of ground clutter present.

Once ϕ_0 is determined, it can be saved as a correction table and referenced when processing incoming data to remove the radar's contributions to the Ψ_{DP} observable before applying the PIA corrections.

4.1.1.2 Applied to Data

After determining the azimuth dependent ϕ_0 and solving for ϕ_{DP}, can apply equation 4.1 to determine the Path Integrated Attenuation. In our assumption, the path

leading away from the radar and its return trip are the same, thus our value is the attenuation of the total trip, and double the attenuation of the 1-way journey.
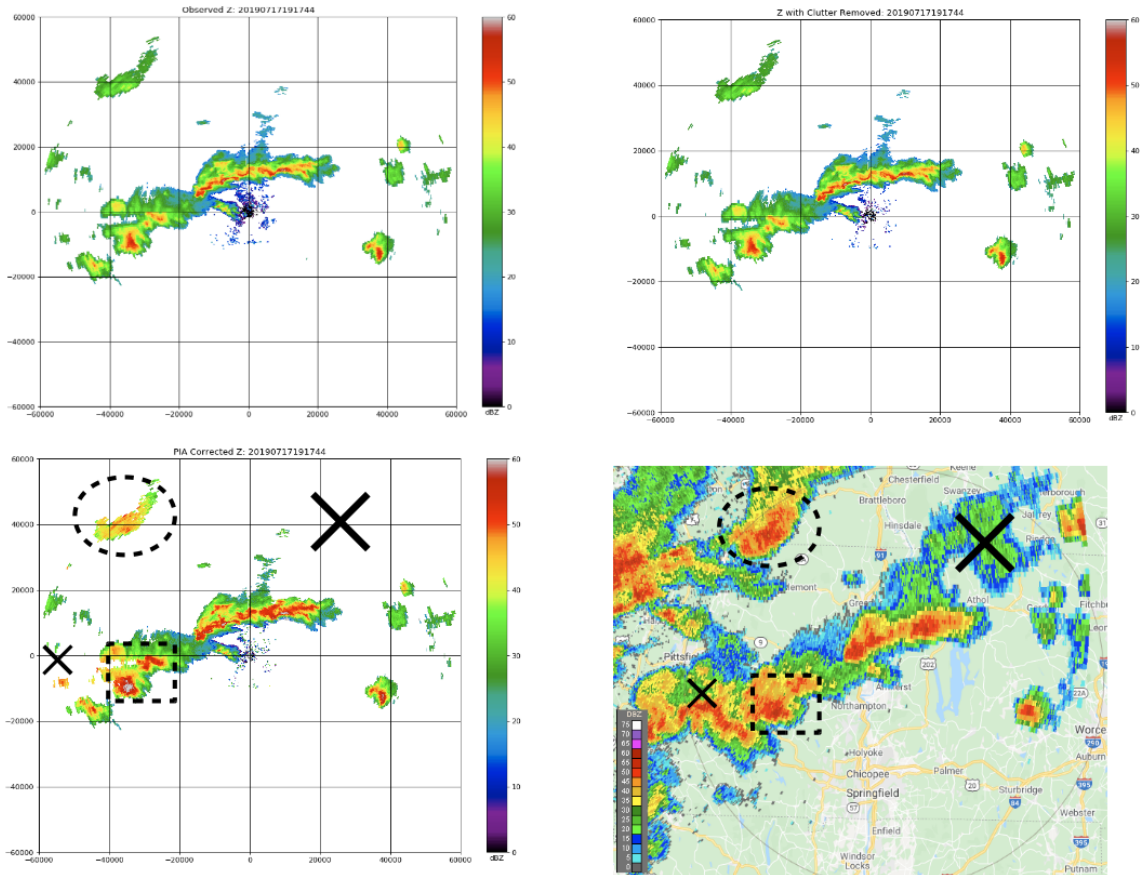
Figure 4.2: PIA correction: Demonstration of PIA corrections applied. Top left shows observed data at 4 deg tilt angle. Top right shows corrections after ground clutter removed and beam blockage corrected (minimal at this tilt). Bottom left shows the corrected data. Bottom right shows separate WSR-88D's view of same weather event. Dotted shapes and X's intended to show corresponding regions of precipitation.

In Fig (4.2), on can see qualitatively how the PIA correction brings UMAXX's data set closer to its neighboring WSR-88D's perspective of the storm. As mentioned previously, the NEXRAD network's data sets will be taken as "calibrated" and will be the standard with which UMAXX's data is compared throughout this paper.

Note the areas enclosed by the dotted circle (square) in either figure are objectively much closer in value than in the original, observed data. It is important to continue

to keep in mind that some data is sufficiently blocked/attenuated such that it is irretrievable as indicated by the bold $\boldsymbol{X}$'s.

4.1.2 NEXRAD Comparison

To validate these attempts in correcting for signal attenuation and beam blockage, data streamed from nearby radars in the NEXRAD network is leveraged. By calculating overlapping regions in the UMAXX and Albany (KENX) radar's scan strategies, one can analyze approximately adjacent range bin pairs from each radar. In the context of reflectivity factor, the range bin pairs would ideally exhibit a 1-to-1 relation given the two radars are well calibrated. A similar strategy is used in other papers to validate corrections when another radar in reasonable proximity is available to serve as a baseline ([14]).

When collecting range bin pairs, the ideal set of conditions would be the pairs were observed at the exact same time and at the exact same altitude. However, in the interest of obtaining sufficient data points for meaningful incite, we assume there exists a duration of time and a range in altitude within which the precipitation experiences minimal variation. For our purposes, it was empirically determined that 15 seconds and 200 meters were appropriate constraints to achieve visibly linear correlation. Hence, a 120 by 120 kilometer square was drawn around the UMAXX radar site and subdivided into 200 meter squares. Each square was populated by object holding KENX and UMAXX reflectivity data as well as time stamps and other supplemental data to achieve reflectivity pairs for comparison.
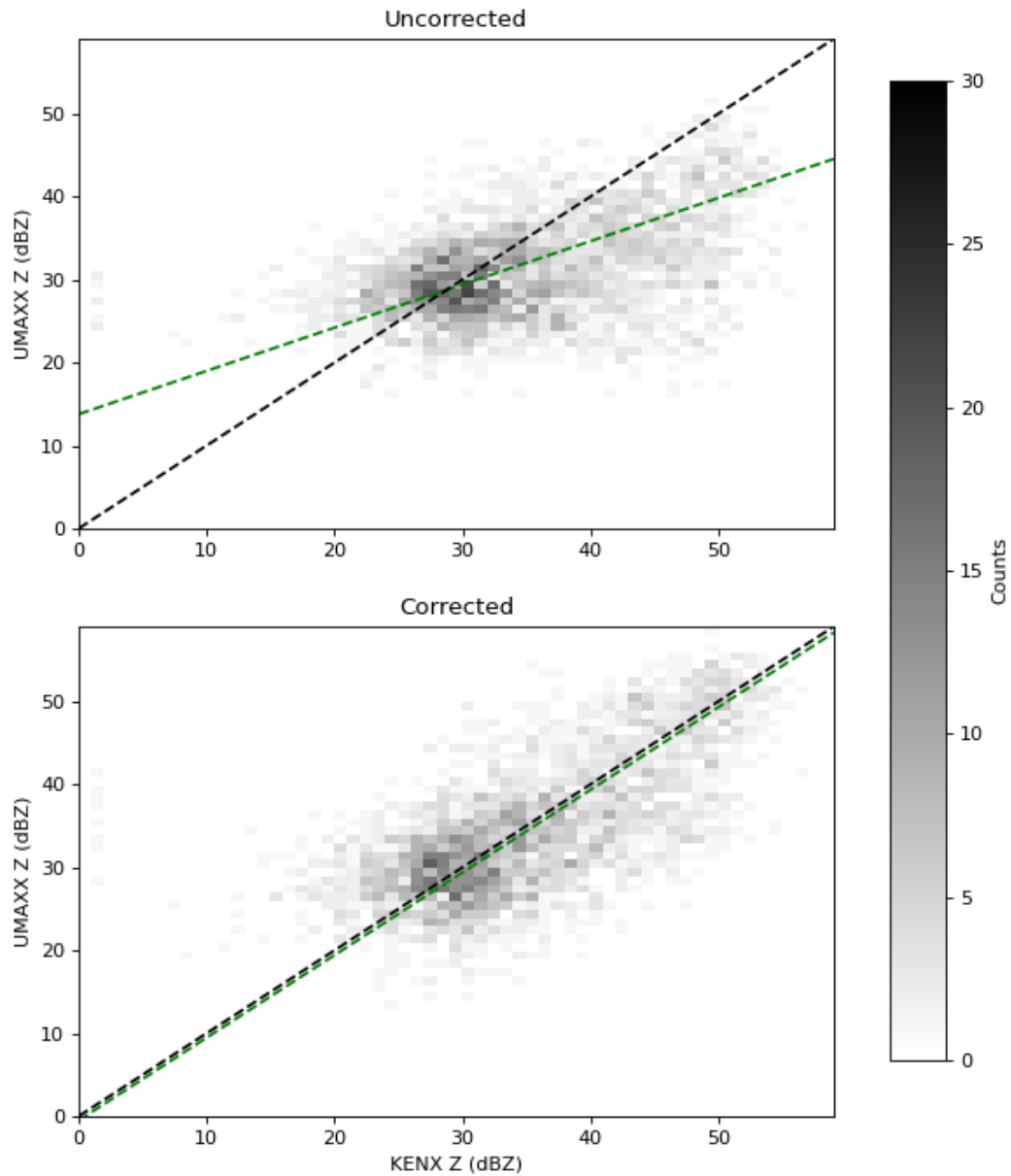
Figure 4.3: **A 2D histogram of single rain event on May 24, 2019 is analyzed**
Top: Shows comparison in dBZ of KENX and the uncalibrated UMAXX radar in
overlapping regions of space. The dashed diagonal line shows the ideal, 1-to-1 relation.
Bottom: After applying the PIA calibration and beam blockage corrections, Note how
UMAXX data aligns itself with the KENX along the dashed, 1-to-1 line.

In Fig 4.3, a green regression line is generated to illustrate the relation between the range bin pairs. A slope less (more) than 1 would indicate the UMAXX is under (over) compensating for the effects of attenuation and beam blockage. Note the regression line is partially below dashed 1-to-1 line. This indicates the UMAXX radar could be running somewhat "cold" in comparison to KENX. Recall from 2.6 The reflectivity constant R_c is made up of a variety of constants including gain of the antenna. If regression line were consistently below 1-to-1 line across many data sets, the source of the offset could be within this value.

4.1.3 Wet Radome Attenuation Analysis

Another issue that impacts the reflectivity measurement is when water collects on the radome's outer surface due to rain directly overhead. It is assumed with older radomes that the hydrophobic coating on the radome's surface degrades and an approximately uniform layer of water forms. This layer of water on the radome attenuates the radar's signal thus degrading the sensitivity of the system.

It has been investigated and shown that this additional boundary contributes to the brightness temperature of the radar's antenna [11]. This increase in noise temperature can be quantified and thus mapped to an attenuation that is then attributed to the microwave emission of distant storms as well as the water layer collected on the radome. This section outlines the process that attempts to untangle these two contributing noise sources with the overarching goal of solving for the wet radome attenuation.

4.1.3.1 Calibrating Noise

The concept of monitoring the brightness temperature of the UMAXX antenna essentially involves using the radar as a radiometer. Radiometer's are ultra sensitive remote sensing devices used to measure and detect changes in the microwave emission of a given environment. As such, they require frequent calibration to ensure drift in

system temperature and performance of components do not contaminate the measurements. Presently, this is not implemented in the UMAXX's scan strategy, thus some crude calibration measures are taken in an attempt to perform this analysis.
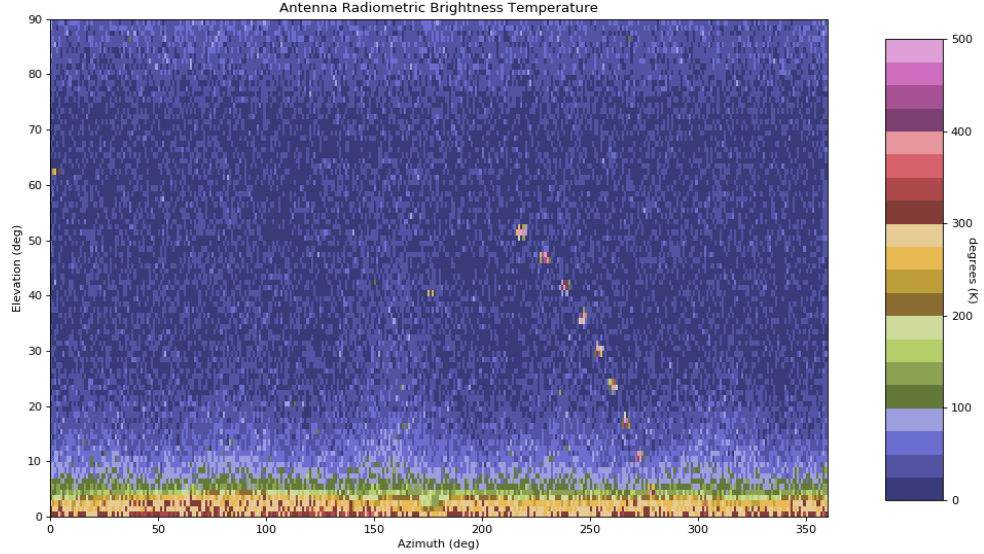
Figure 4.4: This figure shows UMAXX data collected over the course of an afternoon on receive only. At the low elevations the radiometer is observing higher temperatures due to the higher brightness temperature emitting from the ground clutter. At various points the sun is also observed sporadically throughout the day. Temperatures are related to A/D voltages by making assumptions based upon the well understood clear sky and sun temperatures.

Above in Fig (4.4), the plot shows the median noise value along each radial for each elevation angle. Using well understood values of brightness temperature for the sun and the sky at X-band, the radar's receiver is able to be calibrated to measure the brightness temperature of the surrounding environment. The result is a linear equation which maps the noise power from the ADC to a brightness temperature as follows:

$$m = \frac{T_{hot} - T_{cold}}{p_{sun} - p_{sky}} \qquad (4.3)$$

$$b = T_{cold} - m \times p_{sky} \tag{4.4}$$

where m is the slope and b is intercept. p_{sky} is the noise power received when observing just the sky (minimal emission from ground or other targets and surfaces) and T_{cold} is the corresponding brightness seen by the sky at X-band which is $\approx 10K$. p_{sun} is the noise power received when the sun is within the region of UMAXX's main beam and T_{hot} is the corresponding brightness temperature which can be calculated as follows

$$T_{hot} = \left(\frac{\theta^2_{sun}}{\theta^2_{umaxx}} \right) T_{sun} + \left(1 - \frac{\theta^2_{sun}}{\theta^2_{umaxx}} \right) T_{sky} \tag{4.5}$$

where θ_{sun} is the angle subtended by the sun, θ_{umaxx} is beam width of UMAXX's main beam, and T_{sun} is the temperature of the Sun ($\approx 5778K$).

The effects of the dry radome itself also need to be considered. While the loss of the radome (L) isn't precisely known, .3 dB is currently used as a typical value to be expected for radome material. The below equations apply the corresponding self-emission ($e = 1 - \frac{1}{L}$) and transmission coefficient ($t = \frac{1}{L}$) to T_{hot} and T_{cold}

$$T'_{hot} = tT_{hot} + e290 \tag{4.6}$$

$$T'_{cold} = tT_{cold} + e290 \tag{4.7}$$

Where 290 K is the radome's assumed temperature. The new resulting linear equation is defined as

$$m' = \frac{T'_{hot} - T'_{cold}}{p_{hot} - p_{cold}} \tag{4.8}$$

$$b' = T'_{cold} - m'p_{sky} \tag{4.9}$$

Using this linear equation, the data set from Figure 4.4 can then be generated by mapping the received noise power to a corresponding antenna radiometric temperature. Can also use t and e to compensate for the absorption and emission of the dry radome and yield a brightness temperature closer to the truer value:

$$T_{meas} = \frac{T'_{meas} - e290}{t} \qquad (4.10)$$

Where T_{meas} is the brightness temperature of the target and T'_{meas} is the antenna temperature. Going forward, when discussing brightness temperatures measured by the radar, it is implied that T_{meas} is being used.

Considering it would be infeasible to run this calibration during normal operation, we instead elect to use this data set as our assumed benchmark to recalibrate UMAXX on a given day. Using an interval of the day in which no weather is present, the radar's scan at 1 degree tilt and 6 degree tilt are used as the new hot and cold targets, respectively. The corresponding T_{hot} and T_{cold} are taken to be the median value along each tilt found in the above receive-only data set (110K and 30K, respectively).

This method of calibration does have the potential for error, but will be useful for the explicit purpose of detecting a relationship between the water on the radome and the resulting increase in microwave emission. For an implemented radome attenuation correction process, the UMAXX scan strategy would be modified to include a known injected noise source periodically to recalibrate throughout data collection; much like in a traditional radiometer. With a method of calibrating the receiver's noise factor established, the next step is to begin looking at data featuring weather.

4.1.3.2 Noise Contribution of Distant Storms

One challenge with this proposed method is that when water has collected on the radome, more often than not there will be a storm present as well. This storm will have its own microwave emission that will contribute to the rise in noise floor.

Unfortunately, looking at the noise floor alone it is impossible to untangle the joint contributions from the distant storm and the wet radome. Recall from section 4.1.1 that it was demonstrated that the outlined PIA method utilizing ϕ_{DP} was effective in determining the attenuation of the radar's signal due to rain. Therefore, it is explored in this subsection if one can achieve a comparable total attenuation value from the distant storm via analyzing the changes in the noise floor resulting from the increased microwave emission. This will be done using periods of time where rain is present in the region while the radome itself is dry to ensure the predominant contribution to rises in the noise floor is from the distant storm. The goal in this section is to show that calculating the loss of distant storms using ϕ_{DP} is comparable to when measured using the noise floor. This will build the case that using ϕ_{DP} is a viable option to help isolate the wet radome's contribution to the fluctuations in the noise floor measurement.
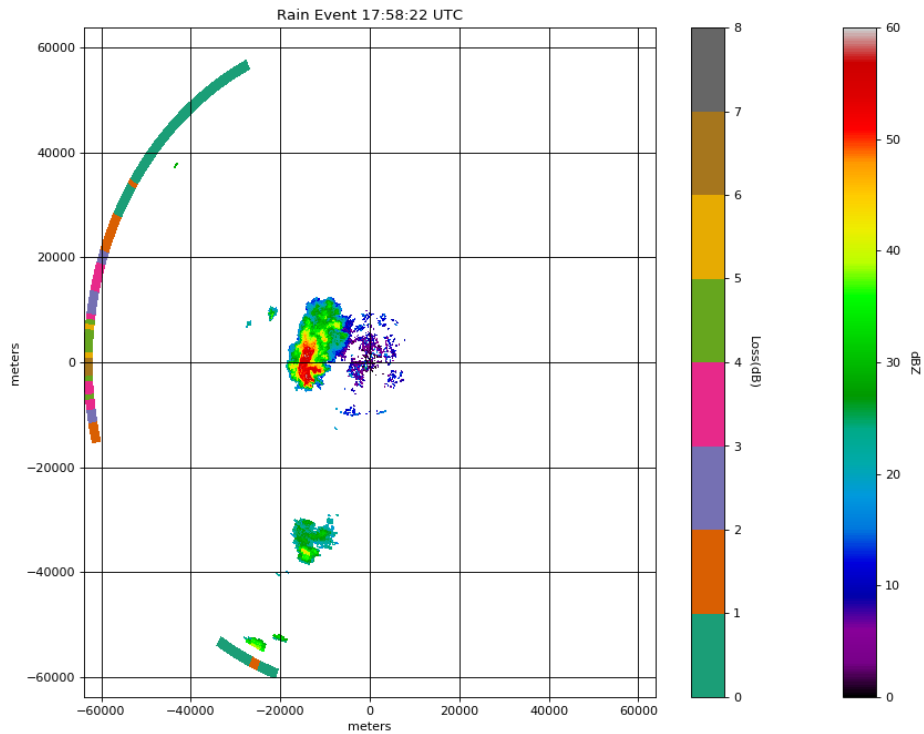
Figure 4.5: This plot shows the reflectivity of a data frame collected for a storm on July 27, 2019. The outer ring of discrete color mappings shows the total 1-way attenuation along each radial as calculated using the ϕ_{dp} method.

In the Figure (4.5) above, an approaching storm is observed and the total attenuation along each radial is displayed in the outer ring. This is calculated by using the ϕ_{DP} method and then divided by 2 to represent the 1-way attenuation. This scan serves as a good starting point as it features an isolated storm yet no precipitation has had a chance to collect on the radome.
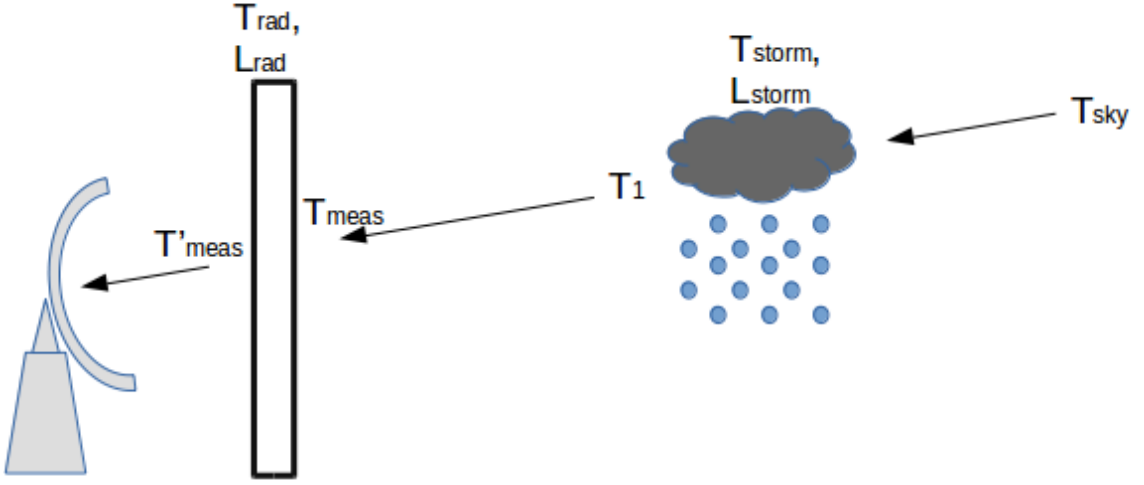
Figure 4.6: This image illustrates how UMAXX perceives the noise temperature of a distant storm.

By considering the storm and background sky as a two-element network, UMAXX was used as a means of measuring the noise temperature at the port closest to the radar, T_1. In this instance, $T_1 = T_{meas}$ is the noise temperature as measured by UMAXX after removing effects of dry radome. In looking at the problem this way, one can write T_1 in terms of the temperature, T^p_{storm} and loss L_{storm} of the storm as well as the temperature of the atmospheric background, T_{sky} as was done in equations 4.6 and 4.7:

$$T_1 = \left(1 - \frac{1}{L_{storm}}\right) T^p_{storm} + \frac{T_{sky}}{L_{storm}} \tag{4.11}$$

It is now possible to solve for the loss, L_{storm}:

$$L_{storm} = \frac{T_{sky} - T^p_{storm}}{T_1 - T^p_{storm}} \tag{4.12}$$

Where we approximate the physical temperature T^p_{storm} as $280K$. The storm's physical temperature is likely somewhere between 270 and 290 so choosing 280K ensures an error in 1-way storm attenuation of $< .6$ dB.

Below, in Figure 4.7, the noise floor is recorded earlier in the day with no rain present and then again later when storm is approaching. The top plot features the data with no weather present averaged over the course of three hours to ensure the median temperature is captured for each radial, this is our T_{sky} in equation 4.12. Then the rain event is observed (bottom of Fig 4.7) as it approaches the radome and serves as T_1. The same day is utilized in an attempt to minimize effects of drift in system noise.
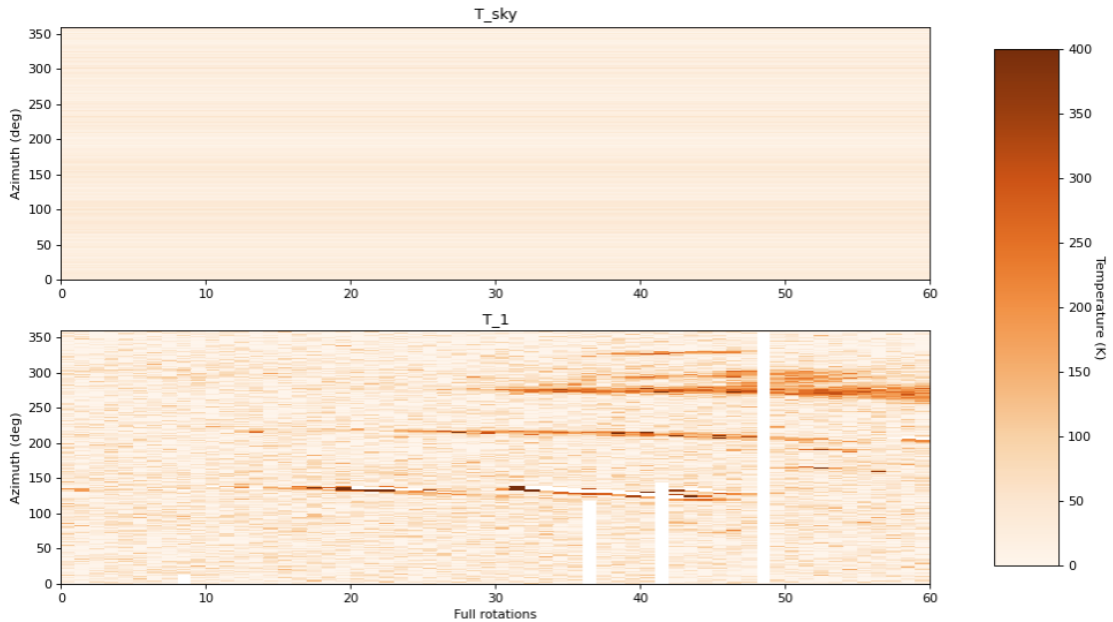
Figure 4.7: Top: the median noise floor value is taken along each radial over the course of three hours. The fluctuations can be attributed to the panels as well as physical temperature of the radome material. Bottom: A storm is observed over three hours as it approaches the radar. Blank data points represent either missing data or when weather is present at the furthest points of the radial. The gray masses are the storm as it travels across UMAXX's scan region.

Using the values obtained in Figure 4.7 with equation 4.12, one can now calculate the attenuation due to the storm along each radial via fluctuations detected in the noise floor. Below, is an analogous plot to Fig 4.5 replaced with results using brightness temperature to calculate the attenuation of the storm.
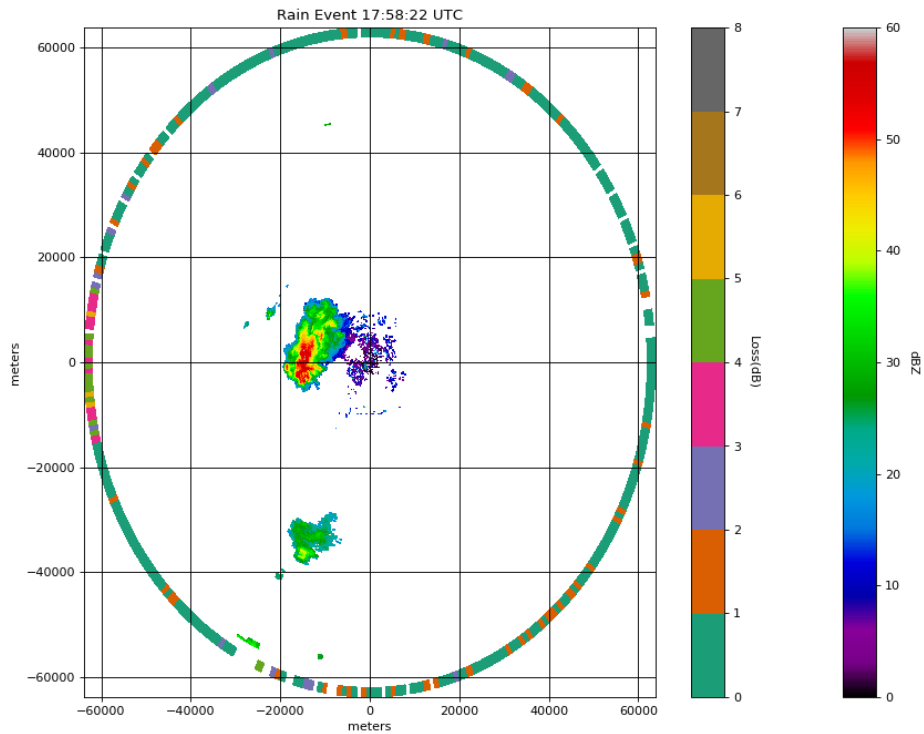
Figure 4.8: This plot shows the same dataframe as Fig 4.5 but with attenuation calculated using the brightness temperature.

We can compare the two methods more directly: focusing on the sector ranging from 180 to 360 degrees in azimuth shown in Figure 4.9a is the two methods and how they track each other. While the the microwave emission method appears to mimic the ϕ_{DP} method, it features significant variance. Throughout the course of this rain event, the data obtained from either method was compared in the 2D histogram format to help visualize the trend with a larger collection of data (Figure 4.9b).
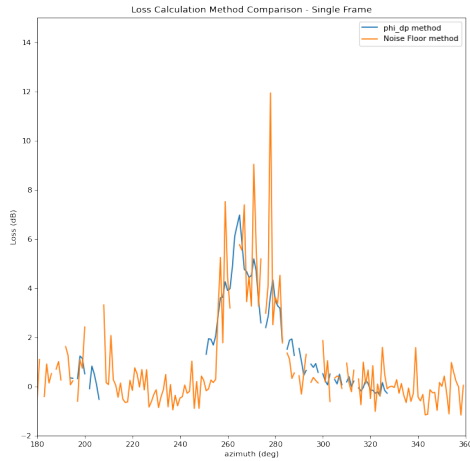
(a) This plot shows the 180 to 360 degree sector of the data frame featured in Fig 4.5 and 4.8 with both the ϕ_{DP} and the noise figure method displayed. While the two methods appear to track each other, the values derived from the noise floor method features greater variance.
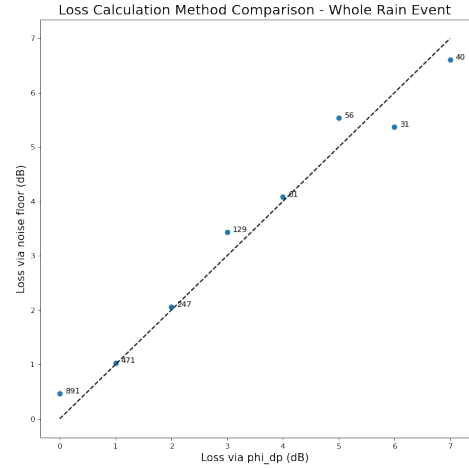
(b) This plot shows an average of loss as calculated by interpretting the noise floor. The averages are binned along the x-axis by the corresponding loss calculated by ϕ_{DP}. The raw loss pairs are highly variant, but the averages show a strong 1-to-1 correlation as indicated by the dashed line.

The high variance in loss calculated via the noise floor analysis can be mitigated by increasing samples in the absence of a transmit pulse/echo. Presently, the final 10 range bins are sampled of each pulse and checked for a transmit echo. If no echo is present then the received power is taken to be the antenna brightness temperature. Either increasing this number of samples or disabling the transmitter for one pulse period would serve to increase stability of this measurement.

Using these results from Figure 4.9b, it is inferred that the two methods of calculating the total loss along a radial due to an approaching storm are interchangeable. This conclusion will be useful in the following section when water on the radome is considered.

4.1.3.3 Extracting Radome Attenuation

With a better understanding of how the presence of a distant storm impacts the noise floor, the next step is to look at the presence of both distant storms and water over the radome and attempt to extract the attenuation due to the wet radome. The storm and atmospheric background will still be regarded as a two-element network, but for this part of the analysis L_{storm} is determined from the ϕ_{DP} method. Using the relation derived from 4.9b, the attenuation determined from ϕ_{DP} is converted to a noise temperature and then used to solve for T_1 in equation 4.11. This is necessary because as shown in Figure 4.10, with the addition of the water layer on the radome T_1 is no longer the noise temperature measured by UMAXX. Instead, T_1 is the emission incident upon the wet radome before being subject to the transmission and self emission of the water layer.
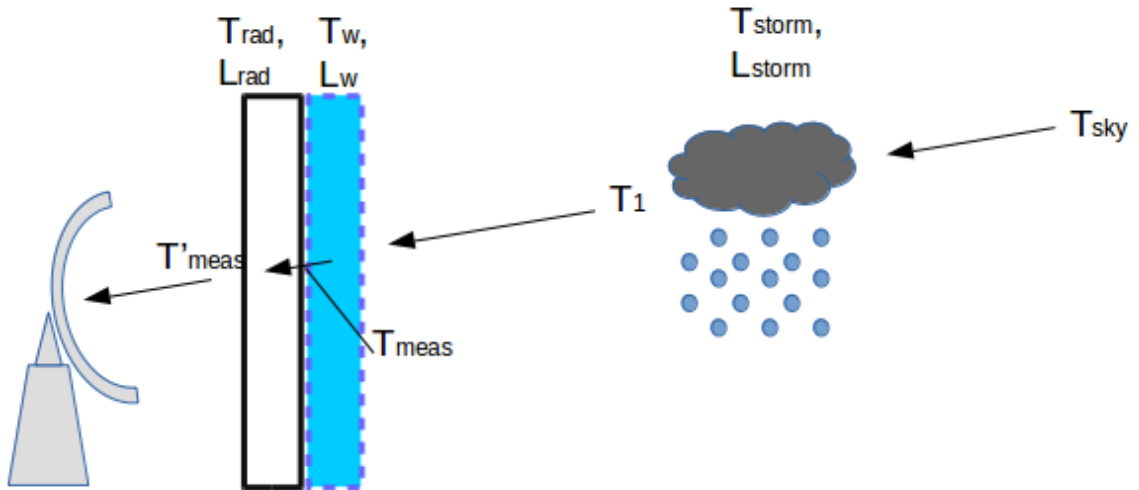

Figure 4.10: This image illustrates how UMAXX perceives the noise temperature of a distant storm with the presence of water on the radome.

To account for the effects of the additional lossy layer, one can modify Equation 4.11 to add in a new stage that represents the water collected on the radome:

49

$$T_{meas} = \left(1 - \frac{1}{L_w}\right) T_w^p + \frac{1}{L_w} \left[\left(1 - \frac{1}{L_{storm}^\phi}\right) T_{storm}^p + \frac{T_{sky}}{L_{storm}^\phi}\right] \qquad (4.13)$$

Note, in equation 4.13 the section inside the square brackets is analogous to equation 4.11. The addition of the ϕ in the superscript indicates the loss was determined using the ϕ_{DP} method. Can thus re-write as

$$T_{meas} = \left(1 - \frac{1}{L_w}\right) T_w^p + \frac{1}{L_w} \left[T_1^\phi\right] \qquad (4.14)$$

Lastly, with an equation in the same form as 4.11, L_w can be found as follows

$$L_w = \frac{T_1^\phi - T_w^p}{T_{meas} - T_w^p} \qquad (4.15)$$

Where the physical temperature of the water on the radome is approximated to be $T_w^p = 290K$. As can be seen, this method relies on using ϕ_{DP} to calculate the noise temperature of the environment incident upon the wet radome.

4.1.3.4   Method Validation

To validate this method, reflectivity close to the radar was used as a means to approximate the rain rate in the region over the radar. These Z data points were then compared with the radome loss calculated via the microwave emission. As shown in Figure 4.11a, there is a clear correlation between the two variables, ie Z close to the radar and the wet radome attenuation.

The results were further compared in 4.11b with those of Frasier, et al [14]. The relation to rain rate and wet radome attenuation was empirically derived via inter-radar comparisons in the French Alps. While the results of either study yield similar values of attenuation for a given rain rate, the polynomial equations describing the results are slightly different in nature. Note the radars from the Frasier study are in a starkly different environment situated in the French Alps. Additionally, the radome from that study is approximately spherical as opposed to the UMAXX's cylindrical

side walls. These considerations alone make the differing nature of the polynomials in Figure 4.11b unsurpising.

With a linear relation fit to the points, one would expect a y-intercept of 0. That is, with no rain there should be no excess radome attenuation to account for. A nonzero intercept (as seen in Figure 4.11a) could result from several factors. There could be an error in our approximation of the loss of the radome, the precise noise temperature of the T_{hot} or T_{cold} calibration points, the attenuation scale factor a used to isolate the microwave emission from the distant storm, or an overall offset due to the variance that exists in the noise floor measurement. The source of this nonzero intercept can be more precisely attributed and corrected for by implementing a more stable noise calibration procedure, refining the scale factor, a, and increasing the number of noise floor samples.
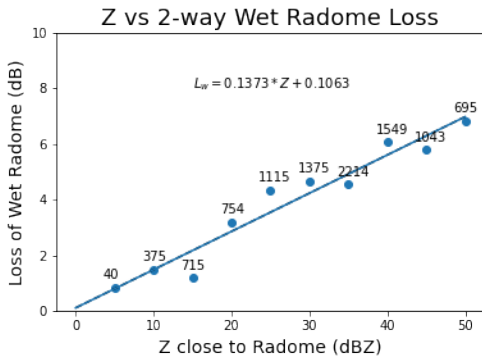
(a) Reflectivity close to the radar plotted vs the two way radome attenuation. The data was averaged to help determine trend. The numeric label indicates numbers of samples comprising each data point.
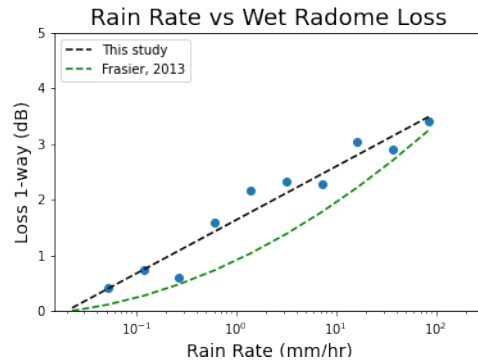
(b) 1 way radome loss shown as a function of rain rate. Results are compared with findings from Frasier et al, 2013.

The findings of this thesis represent a single case from a storm that passed overhead the UMAXX site on August 18, 2019. Due to the unstable nature of the calibration process available and utilized, it wasn't prudent to compile multiple rain events to represent a single trend. The conclusion to be made from this section is that it is effective to derive, quantitatively, the attenuation effects of a wet radome using

the microwave emission of the sheet of water. With a stable and consistent noise calibration process, it would be feasible to use the method outlined here to implement a radome attenuation correction procedure during normal operation.

4.2   Differential Reflectivity Calibration

There are two sources of bias when looking at Differential Reflectivity (Z_{DR}) that are addressed in this section. First, like reflectivity, Z_{DR} is subject to attenuation when in heavy rainfall. For Z_{DR} this is referred to as *differential attenuation.* As demonstrated in Sec 4.1.1, an attenuation coefficient can be used to scale our ϕ_{DP} as an attenuation correction [9]. This is explained and illustrated further in the following subsection.

In addition to differential attenuation, there are biases internal to the system that need to be calibrated out of the measurement. There exists several methods that have been examined to correct for this. Two are discussed in this section: the vertical (or birdbath) scan and the observation during light (20-22 dBZ) rainfall.

As a means of validating that our Z_{DR} has improved due to these corrections, we utilize what's known as a Membership Function [4] relating Z to Z_{DR}. In this way, we use the verified Z to confirm our corrected Z_{DR} has improved.

4.2.1   Differential Attenuation

Like reflectivity, Z_{DR} is subject to attenuation when heavy rainfall is present, albeit to a lesser degree of severity. Recall from 2.17 that Z_{DR} is a ratio between the vertical and horizontal polarization channels. If the two channels had identical propagation paths, Z_{DR} measurements would not experience attenuation. However, as explained in section (4.1.1), the horizontal channel propagates through an electrically longer path due to geometric shape of rain droplets in heavy rain, thus experiencing more severe attenuation. Similar to Reflectivity Factor, a coefficient was empirically

derived to scale ϕ_{DP} to correct for this attenuation. According to Yu [9], the co-efficient $a = .032$ fits the data well and thus will be used to correct for differential attenuation in this paper.

4.2.2 Calibrating for System Bias

4.2.2.1 Birdbath Scan

First and perhaps most notable method of correcting for Z_{DR} is the vertical, or "birdbath," scan. As the name implies, the radar is set to 90 degrees and scans during light rain (20-30 dBZ). This method assumes that when observed from directly underneath, rain drops are essentially symmetrical and will appear as spheres. As explained in section 2.2.2.1, spheres should yield a Z_{DR} of 0 dB. Also, by rotating radar dish during scan, any asymmetries that could exist due to factors such as wind are further mitigated. In this scan, because the vertical and horizontal polarized channels will be observing the same conditions, there should be no difference in Z_h or Z_v and thus a Z_{DR} of 0 dB is expected. If there is some bias inherent in the system it will make itself apparent in some offset from 0 dB.
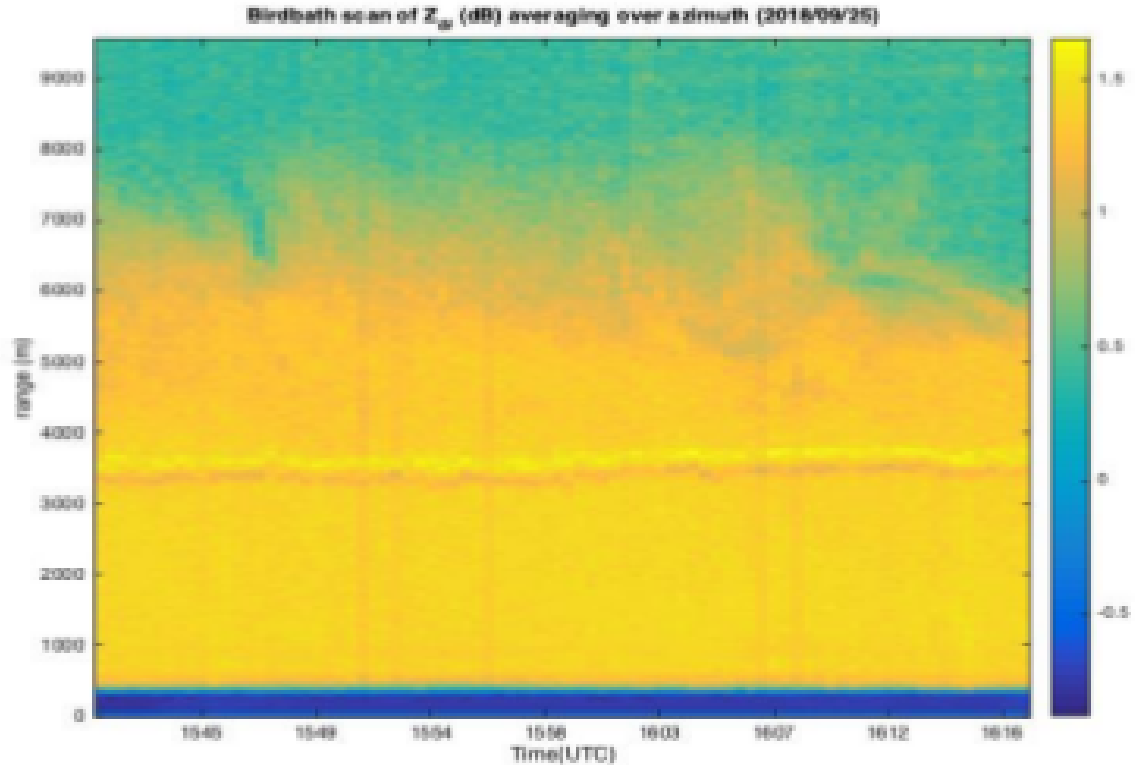
Figure 4.12: Birdbath Scan ZDR plot (Image from Sanchez, et al [12]): x-axis shows times, y-axis shows range (or height above the radar), and color bar indicates Z_{DR} in dB. The yellow, nonzero results suggest the radar is biased positive.

Two disadvantages of this method are as follows. First, it requires interrupting the radar's normal scan procedure to collect the vertical-pointing scan data. A minor inconvenience, but nonetheless having a method available that utilizes data collected during normal operation would be useful if one wished to perform more frequent calibrations or if retroactively confirming the validity of a calibration in an older data set was needed.

Second, the birdbath method assumes there is no azimuth-based dependence for Z_{DR} bias. As will be demonstrated here and has been shown elsewhere [6], the radome has considerable influence over the bias which results in an azimuth dependence that is worthwhile to mitigate against.

54

4.2.3 Light Rain Observations During Normal Scan Strategy

A method that answers the above concerns is by analyzing rainfall data collected during light rain under normal scanning procedure. As explained in [6] and [10], it can be assumed that rain droplets within a range bin that is exhibiting a reflectivity within 20-22 dBZ is very close to spherical and hence a Z_{DR} of $\approx$ .2 dB is expected. Figure 4.13 shows an average of several rain events throughout the month of July at the four tilt angles.
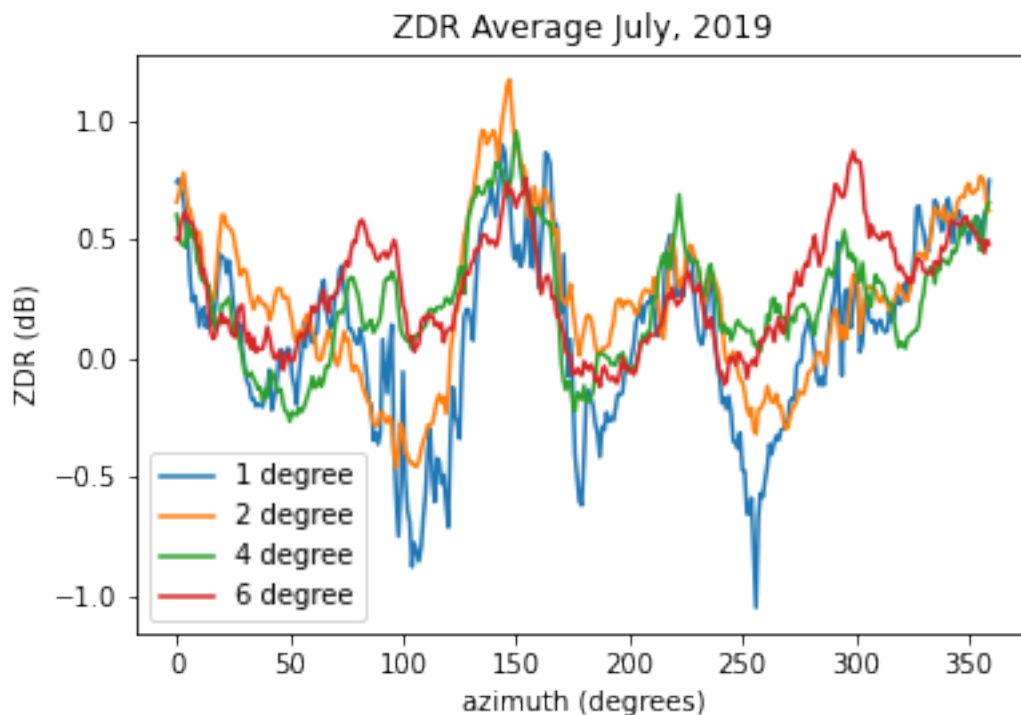
Figure 4.13: Light Rain ZDR averaging: Data for light rain (20-22 dBz) taken over the course of several rain events throughout July, 2019. ZDR data taken near the radar was binned by azimuth and averaged. At the higher tilts, 5 peaks can be made out which likely correlate with the five panels that make up the radome.

There are several restrictions that need to be placed on these data sets to ensure the quality of the data. ρ_{HV} should be limited to $> .99$ to restrict range bins to purely rain drops. Additionally, to limit effects of differential attenuation, we will restrict

range to a maximum distance of 5 km. These are comparable restrictions to those in Ventura et al [6].

4.2.4 Results

Shown in Fig 4.14 is a storm on 19 May, 2019. the uncorrected data has windmill-like pattern aligned with radials of the radar. This can be attributed to the peaks/troughs we see in the calibration data set when applying corrections, the patterns are resolved and a Z_{DR} plot that is more consistent with reflectivity data is the result.

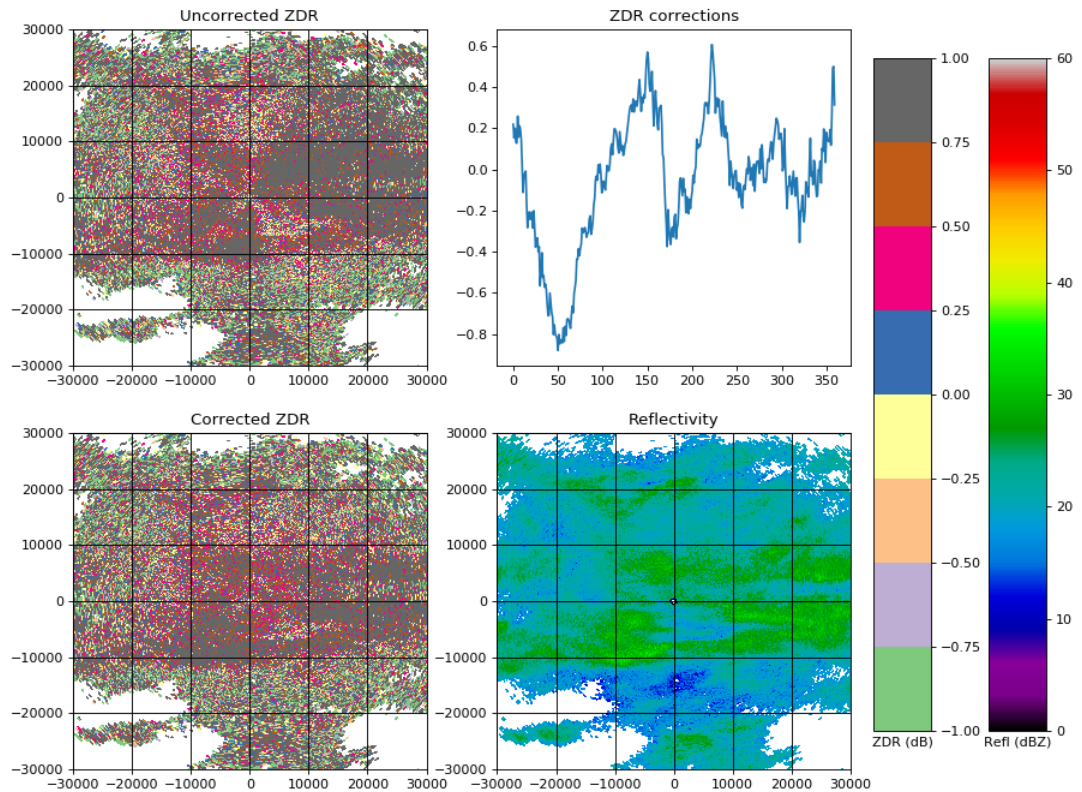Figure 4.14: Corrections Applied to Z_{DR} Data at 4 deg tilt: In top left, uncorrected Z_{DR} data exhibits "windmill" pattern suggesting azimuthal bias in system. After applying PIA corrections as well as Z_{DR} bias corrections (top right) the resulting corrected data is displayed in bottom left. Note the corrected Z_{DR} data is more typical of what could be expected based on Reflectivity data shown in bottom right.

Fig 4.14 helps see from a qualitative perspective how Z_{DR} benefits from these corrective measures. However to verify in a more concrete sense, can compare Z_{DR} against the corrected reflectivity using what's known as *membership functions* (H. Al-Sakka, et all [4]). Essentially these functions were developed to better understand the relation between various radar products in different categories of precipitation. For our purposes they will serve to illustrate that Z_{DR} measurements have improved as a result of the corrections illustrated above.

Membership Function $Z_{DR} = f(Z_H)$ for X-Band
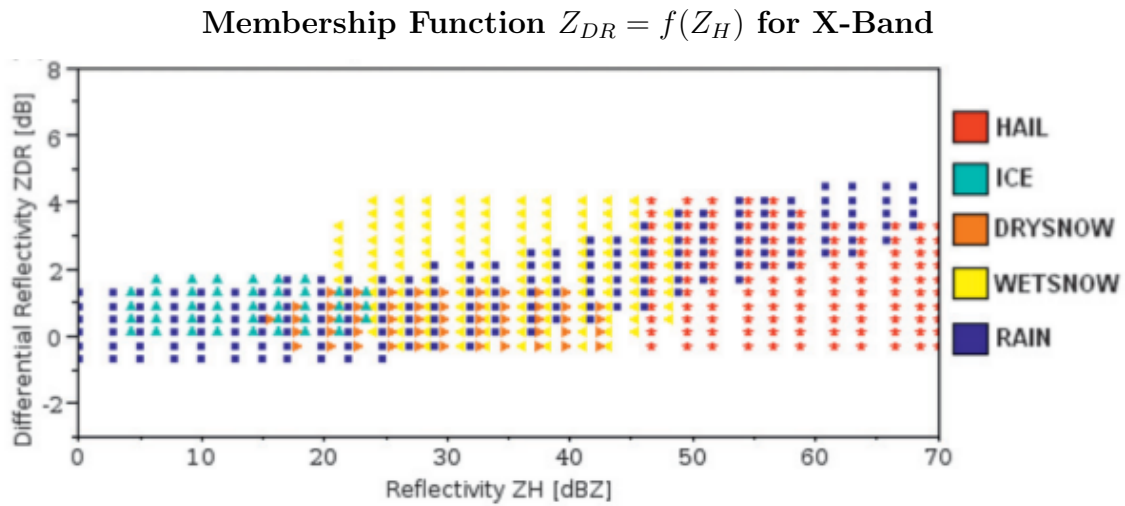
Figure 4.15: Reflectivity vs Z_{DR} at X-Band (figure from Al-Sakka et al [4]): Shows how Z relates to Z_{DR} for various forms of precipitation. This thesis is interested specifically in Z vs Z_{DR} in rain (dark blue).

For UMAXX, one can see in Figure 4.16 that the corrected reflectivity factor and Z_{DR} data fits in well with the range provided by [4]. This compares well against the uncorrected version of the data set and indicates that the calibrations performed for both reflectivity factor and differential reflectivity aided in improving accuracy and consistency of the data.

Figure 4.16: UMAXX Reflectivity vs Z_{DR}: Uncorrected shows a 2D histogram of reflectivity factor vs Z_{DR} before correcting for ground clutter, beam blockage, attenuation, differential attenuation, or Z_{DR} bias. Corrected shows the same data set with these corrections applied. Comparing both with expected results from 4.15 shows a marked improvement.
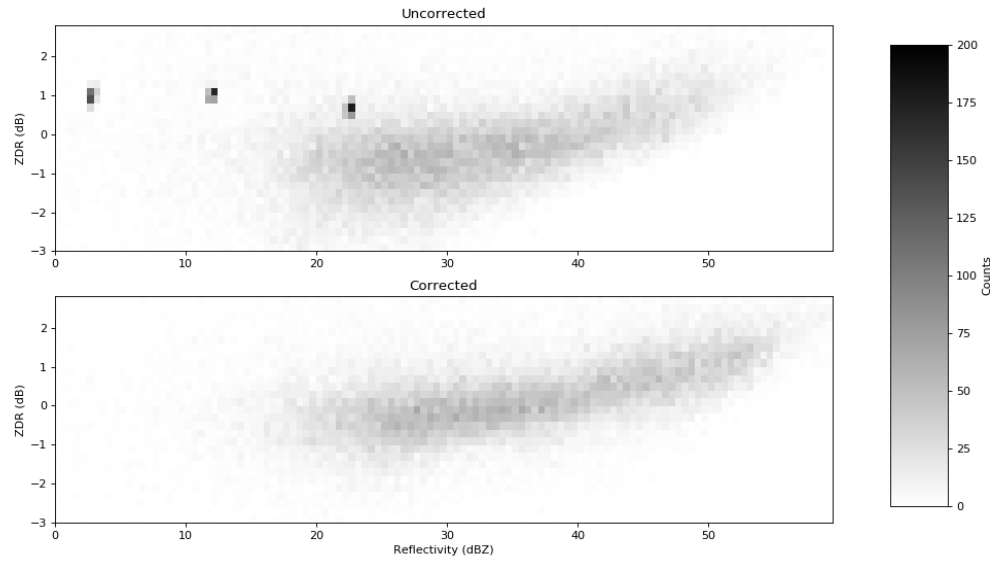
CHAPTER 5

CONCLUSIONS AND FUTURE WORK

This thesis has outlined a path towards taking a previously uncalibrated, dual polarized radar and using various techniques and tools to bring it to a point where it can serve as a reliable system for monitoring meteorological events in the region. By leveraging data available from the NEXRAD network, as well as various assumptions that can be made about the geometric and physical phenomena that exist with terrain and precipitation, the improvements were verified and quantified. With a more concrete understanding of the observables recorded by UMAXX it can now serve its purpose to be used as a reference for Raytheon's SKYLER, as well as aid NWS as it seeks to bolster its ability to monitor meteorological events in the Pioneer Valley region.

While the techniques outlined here aid to calibrate the system and remove biases, there is additional work that can be done to further solidify the integrity of the radar's measurements.

First, the scan time of 30 seconds per tilt limits our time available for processing. This in turn has implications for the complexity and thoroughness of the decision tree classifier. A deeper, more complex tree or perhaps an image classification approach to detect clutter were computationally prohibitive if one wished the data to be streamed in a consistent

Secondly, the methods of radiometric observations need to be improved in order to implement the technique of using the microwave emission of the wet radome to calculate the resulting attenuation value. Additionally, if proven effective, using the

radar as a radiometer to monitor the attenuation of a wet radome will require additional modifications to the system. Typically, in the operation of a radiometer, frequent calibration is employed to maintain the integrity of its measurements. As the radar stands now, the calibration procedure is not consistent and is unstable. It would be worthwhile to consider using a stable noise source to frequently reference so as to correct for drift in the system. Additionally, the signal processor takes the median of the final 10 range bins along a given radial. By increasing the number of samples, one can diminish error in attenuation. One method of doing this is to have a pulse with Transmit off. This has the effect of essentially reducing the dwell time of the radar in lieu of increasing precision of attenuation calculations.

Also, the ϕ_{DP} attenuation coefficients meant to correct for attenuation in reflectivity factor and differential reflectivity were determined and confirmed in differing climates and at different frequencies than UMAXX. While it is confirmed here that the coefficients provided serve to improve the measurements, it could be worthwhile to investigate these values and see if some optimal coefficient could be reached that is uniquely determined for this system and in this region. This could either be done by deriving a coefficient, a independently or by simply adjusting a over many data sets to some optimal value.

Finally, the methods outlined in this thesis generate tables of correction values and system biases to be referenced during the radar's operation. As the radar is subject to seasonal changes, degradation, and other sources of drift, these tables may lose their validity. Implementing a system of more frequent calibration and monitoring for significant drifts in the data could serve to ensure consistency and accuracy of UMAXX's measurements through the years.

BIBLIOGRAPHY

[1] Balanis, Constantine A. *Antenna Theory: Analysis and Design*. Wiley, Hoboken, New Jersey, 2016.

[2] Bringi, V.N., and Chandrasekar, V. *Polarimetric Doppler Weather Radar*. Cambridge University Press, New York, 2001.

[3] Doviak, Richard J., and Zrnić, Duan S. *Doppler Radar and Weather Observations*. Dover, Mineola, New York, 1993.

[4] Hassan Al-Sakka, Abdel-Amin Boumahmoud, Beatrice Fradon Stephen J. Frasier Pierre Tabary. A new fuzzy logic hydrometeor classification scheme applied to the french x-, c-, and s-band polarimetric radar. *Journal of Applied Meteorology and Climatology 52* (2013), 2328–2344.

[5] Jonathon J. Gourley, Pierre Tabary, and du Chatelet, Jacques Parent. Empirical estimation of attenuation from differential propagation phase measurements at c band. *Journal of Applied Meteorology and Climatology 46* (2007), 306–317.

[6] Jordi Figueras Ventura, Abdel-Amin Boumahmoud, Beatrice Fradon Pascale Dupuy Pierre Tabary. Long-term monitoring of french polarimetric radar data quality and evaluation of several polarimetric quantitative precipitation estimators in ideal conditions for operational implementation at c-band. *Quarterly Journal of the Royal Meteorological Society 138* (2012), 2212–2228.

[7] Kumjian, Matthew R. Principles and applications of dual-polarization weather radar. part 1: Description of the polarimetric variables. *Journal of Operational Meteorology 1* (2013), 226–242.

[8] Meischner, Peter. *Weather Radar: Principles and Advanced Applications.* Physics of Earth and Space Sciences. Springer, Germany, 2005.

[9] Nan Yu, Nicolas Gaussiat, Pierre Tabary. Polarimetric x-band weather radars for quantitative precipitation estimation in mountainous regions. *Quarterly Journal of the Royal Meteorological Society 144* (2018), 2603–2619.

[10] Pierre Tabary, Abdel-Amin Boumahmoud, Herve Andrieu Robert J. Thompson Anthony J Illingworth Erwan Le Bouar Jacques Testud. Evaluation of two "integrated" polarimetric quantitative precipitation estimation (qpe) algorithms at c-band. *Journal of Hydrology 405* (2011), 248–260.

[11] R. Thompson, A.Illingworth, T. Darlington, and Ovens, J. Correcting attenuation in operational radars from both heavy rain and the radome using the observed microwave emission. *ERAD* (2012).

[12] Sanchez, Jezabell Vilardell. The umass experimental x-band radar (umaxx): An upgrade of the casa ma-1 radar to support cross-polarization measurements.

[13] Skolnik, Merril I. *Introduction to Radar Systems.* McGraw-Hill, New York, NY, 2001.

[14] Stephen J. Frasier, Fadela Kabeche, Jordi Figueras I. Ventura Hassan Al-Sakka Pierre Tabary. In-place estimation of wet radome attenuation at x-band. *Journal of Atmospheric and Oceanic Technology 30* (2013), 917–928.